










## TOPICAL REVIEW

## Non-linear processes in the extreme ultraviolet

## OPEN ACCESS

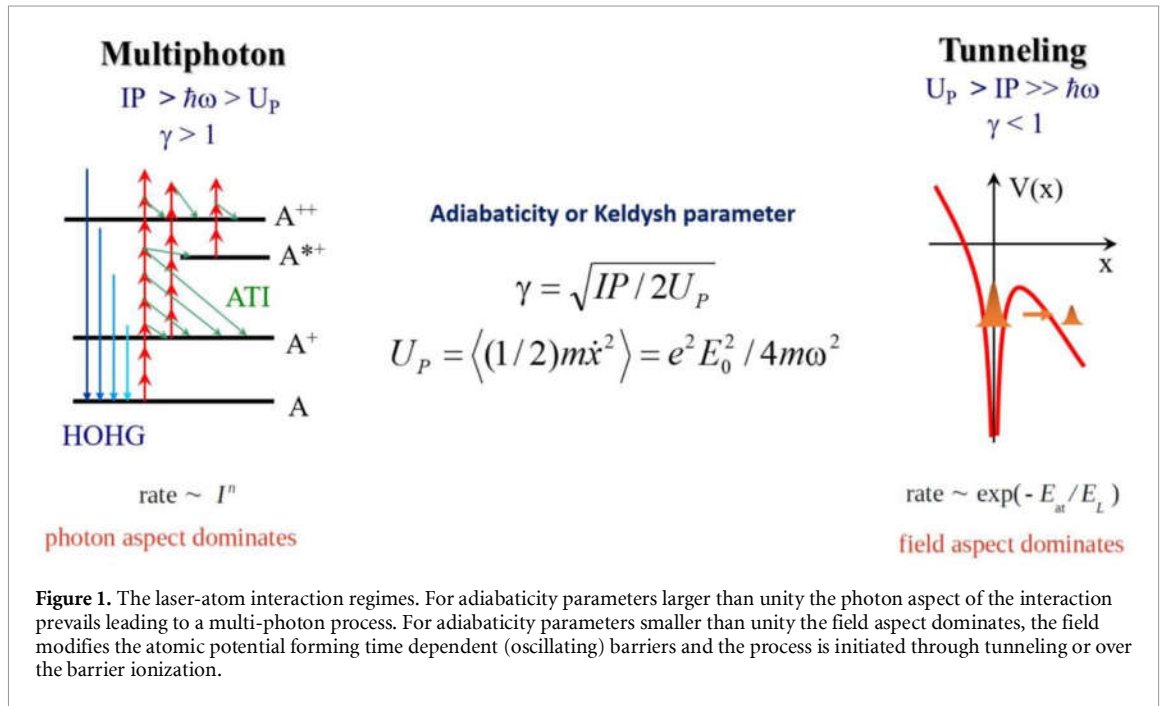
RECEIVED  
13 March 2020REVISED  
9 May 2020ACCEPTED FOR PUBLICATION  
30 June 2020PUBLISHED  
6 August 2020Original content from  
this work may be used  
under the terms of the  
[Creative Commons  
Attribution 4.0 licence](https://creativecommons.org/licenses/by/4.0/).Any further distribution  
of this work must  
maintain attribution to  
the author(s) and the title  
of the work, journal  
citation and DOI.I Orfanos<sup>1,2,9</sup>, I Makos<sup>1,2,9</sup>, I Liontos<sup>1</sup> , E Skantzakis<sup>1</sup> , B Major<sup>3</sup> , A Nayak<sup>3,4</sup>, M Dumergue<sup>3</sup>, S Kühn<sup>3</sup>, S Kahaly<sup>3</sup> , K Varju<sup>3,5</sup> , G Sansone<sup>6</sup>, B Witzel<sup>7</sup>, C Kalpouzos<sup>1</sup>, L A A Nikolopoulos<sup>8</sup> , P Tzallas<sup>1,3</sup>  
and D Charalambidis<sup>1,2,3</sup> <sup>1</sup> Foundation for Research and Technology - Hellas, Institute of Electronic Structure & Laser, PO Box 1527, GR 71110, Heraklion (Crete), Greece<sup>2</sup> Department of Physics, University of Crete, PO Box 2208, GR 71003, Heraklion (Crete), Greece<sup>3</sup> ELI-ALPS, ELI-HU Non-Profit Ltd., Wolfgang Sandner utca 3., Szeged 6728, Hungary<sup>4</sup> Institute of Physics, University of Szeged, Dom tér 9, 6720, Szeged, Hungary<sup>5</sup> Department of Optics and Quantum Electronics, University of Szeged, Dom tér 9, 6720, Szeged, Hungary<sup>6</sup> Physikalisches Institut, Albert-Ludwigs-Universität Freiburg, Stefan-Meier-Str. 19, D-79104, Freiburg, Germany<sup>7</sup> Université Laval, Centre d'Optique, Photonique et Laser (COPL), Québec G1V 0A6, Canada<sup>8</sup> School of Physical Sciences, Dublin City University, Glasnevin, Dublin 9, IrelandE-mail: [chara@iesl.forth.gr](mailto:chara@iesl.forth.gr)**Keywords:** attosecond, extreme ultraviolet-pump-extreme ultraviolet-probe, multiphoton processes, ultrafast phenomena, high-order harmonic generation**Abstract**

Recent developments in extreme ultraviolet (XUV) and x-ray radiation sources have pushed pulse energies and durations to unprecedented levels that opened up the era of non-linear XUV and x-ray optics. In this quest, laser driven high order harmonic generation sources providing attosecond resolution in the XUV spectral region enabled XUV-pump-XUV-probe experiments, while Free Electron Laser research infrastructures offer unique x-ray brilliances for highly non-linear interactions and since recently, they too entered the sub-fs temporal regime. This topical review discusses the conceptual intricacies of non-linear XUV and x-ray processes, addresses experimental particularities and highlights recent applications of such processes with emphasis to laser driven XUV-attosecond source related research.

**1. Introduction to non-linear extreme ultraviolet processes**

Substantial advances in short wavelength pulsed radiation sources, in the last two decades, have allowed pulse energies and durations to reach such levels that non-linear optics experiments in the extreme ultraviolet (XUV) and x-ray spectral domains have become a reality. This has revealed a direction to exciting physics and offers an optimal tool for time domain studies of ultrafast dynamics. While Free Electron Lasers (FELs) are by far the highest peak brightness sources in the soft and hard x-ray regions [1], coherent, laser driven, table top XUV sources have reached comparable peak brightness at shorter pulse durations [2]. Consequently, non-linear XUV optics became an active research field both in the FEL and the laser driven coherent XUV radiation communities, including attosecond scientists. While energetic attosecond pulses have been recently reported by FEL laboratories [3, 4], attosecond applications have been so far demonstrated only in the laser driven High-order Harmonic Generation (HHG) sources in the XUV spectral region. In the present manuscript, we review the topic of non-linear XUV processes focusing mainly on recent developments of the laser driven XUV and attosecond source user community. In the introductory section, multi-photon (MP) processes are reviewed with emphasis on the intricacies of the XUV spectral region. In the second section experimental developments towards energetic XUV sources and attosecond applications exploiting solely XUV radiation are presented. In the third section we review recent XUV non-linear applications in the femtosecond (fs) and attosecond temporal regimes.

<sup>9</sup> Equally contributed authors



### 1.1. Tunneling vs multi-photon

An adequate description of the interaction of intense radiation with matter depends on the interplay between the radiation's field-strength, carrier frequency and pulse duration, as well as the ionization energy of the matter species. At low frequencies (infrared and lower) and high radiation field-strengths the atomic/molecular Coulombic potential is severely distorted by the potential of the interaction, and the combined Coulombic and radiation field potentials form a barrier that oscillates with the frequency of the radiation. If the degree of distortion is comparable or larger than the ionization potential, an electron can tunnel through the barrier or escape above it respectively. Since the frequency is low, the potential distortion process is quasi-static and thus the tunneling probability is not negligible. The tunneling rate can be treated, in the appropriate limit, as the DC tunneling ionization rate [5] averaged over a single period of the field. Here the field aspects dominate the interaction process (figure 1 right panel). In the opposite side, at not too high field-strengths and high frequencies (ultra-violet, vacuum ultra-violet, x-rays) the degree of the potential distortion is much lower than the ionization potential, the oscillations are much faster and thus the tunneling probability (or over-the-barrier ionization) is strongly reduced. The interaction is now dominated by the photon aspects of the radiation, namely the interaction leads to MP absorption and eventually to ionization (figure 1 left panel). The ionization rate in that case can be treated through lowest order perturbation theory (LOPT).

The above discussion can be quantified by a parameter known as adiabaticity or Keldysh parameter [6], given by

$$\gamma = \sqrt{IP/2U_p} \quad (1.1.1)$$

IP being the ionization energy and  $U_p$  the so called ponderomotive potential, which is the mean kinetic energy of the oscillation of a free electron interacting with the radiation field

$$U_p = \langle \frac{1}{2}m\dot{x}^2 \rangle = e^2 E_0^2 / 4m\omega^2 \quad (1.1.2)$$

with  $m$ ,  $x$  and  $e$  being the mass, position and charge of the electron respectively and  $E_0$   $\hbar$  and  $\omega$  the field amplitude and radial frequency respectively.

A practical numerical evaluation formula for  $U_p$  is:

$$U_p (\text{eV}) = 9.3 \cdot 10^{-14} \cdot I \left( \frac{W}{\text{cm}^2} \right) \cdot \lambda^2 (\mu\text{m}). \quad (1.1.3)$$

When  $U_p > IP \gg \hbar\omega$  then  $\gamma < 1$  and the strong field interaction leads to tunnel ionization, while when  $IP > \hbar\omega > U_p$  then  $\gamma > 1$  and the interaction and ionization has a MP character. It should be noted that we can safely talk about tunneling or MP only if  $\gamma \ll 1$  or  $\gamma \gg 1$ , respectively.

**Table 1.** Scaling of  $U_p$  with the photon energy.

$\hbar\omega$ (eV)	$\lambda$ ( $\mu\text{m}$ )	$U_p$ (eV) (@ $10^{14}$ W cm $^{-2}$ )	$I$ (W cm $^{-2}$ ) (when $U_p = \hbar\omega$ )	$I$ (W cm $^{-2}$ ) (when $IP = 13.6$ eV = $2 U_p$ )
1	1.242	14.4	$6.97 \cdot 10^{12}$	$4.74 \cdot 10^{13}$
5	0.248	$5.7 \cdot 10^{-1}$	$8.7 \cdot 10^{14}$	$1.18 \cdot 10^{15}$
10	0.124	$1.44 \cdot 10^{-1}$	$6.97 \cdot 10^{15}$	$4.74 \cdot 10^{15}$
50	0.0248	$5.7 \cdot 10^{-3}$	$8.7 \cdot 10^{17}$	$1.18 \cdot 10^{17}$
100	0.0124	$1.44 \cdot 10^{-3}$	$6.97 \cdot 10^{18}$	$4.74 \cdot 10^{17}$
500	0.00248	$5.7 \cdot 10^{-5}$	$8.7 \cdot 10^{20}$	$1.18 \cdot 10^{19}$
1000	0.001242	$1.44 \cdot 10^{-5}$	$6.97 \cdot 10^{21}$	$4.74 \cdot 10^{19}$

Apparently, because  $\gamma$  is inversely proportional to the wavelength the MP character will be more pronounced at short wavelengths. Moreover, increasing the ponderomotive potential, via the field's intensity, has an upper limit set by the depletion of the medium. Indeed, the radiation pulse has a temporal distribution. Even if intensities could be increased limitlessly, ionization would be saturated at the leading edge of the pulse due to the finite rise time of the radiation pulse. Hence, the medium would never 'see' the peak intensity [7] as it would be depleted before the top of the pulse is reached; an effect sometimes referred to as 'The Lambropoulos curse' [8, 9], because it invalidated as non-realistic several fascinating effects predicted in high intensity laser-matter interactions in the 80 s. The large frequency and limited intensity 'seen' by the matter ensure that interactions in the XUV and much more pronounced in the x-ray spectral region, are of MP character.

Table 1 gives some numerical examples of the scaling of the ponderomotive energy with photon energy. The third column gives the ponderomotive energy at  $10^{14}$  W cm $^{-2}$  intensity. The fourth column gives the intensity at which the ponderomotive shift becomes equal to the photon energy and the last column the intensity at which it becomes equal to half the ionization energy. From table 1 one can extract that for photon energies  $\geq 10$  eV,  $\gamma$  becomes  $< 1$  at intensities that the atom/molecule will not be subjected to, unless the interaction is with pulses of very short duration. The role of the pulse duration will be discussed in the next section. In figure 2 the blue curved surface shows the dependence of the Keldysh parameter,  $\gamma$ , on the wavelength and intensity of the radiation, for the case, where the photon energy is about half the ionization energy. The horizontal flat yellow surface consists of all wavelength-intensity value pairs for which  $\gamma = 1$ . As can be seen in this graph the tunneling regime is safely reached at intensities  $> 10^{16}$  W cm $^{-2}$  for 20 eV photons and at higher intensities for larger photon energies. For pulses with durations  $> 0.1$  fs, these intensities are above the atomic/molecular ionization saturation intensity, meaning that the atom/molecule will be essentially fully ionized before the peak intensity is reached. Therefore, one can safely conclude that for photon energies  $\geq 20$  eV and pulse durations  $\geq 0.1$  fs the interaction is of MP character. However, strong field effects become observable in specific cases at the today's available FEL intensities [10].

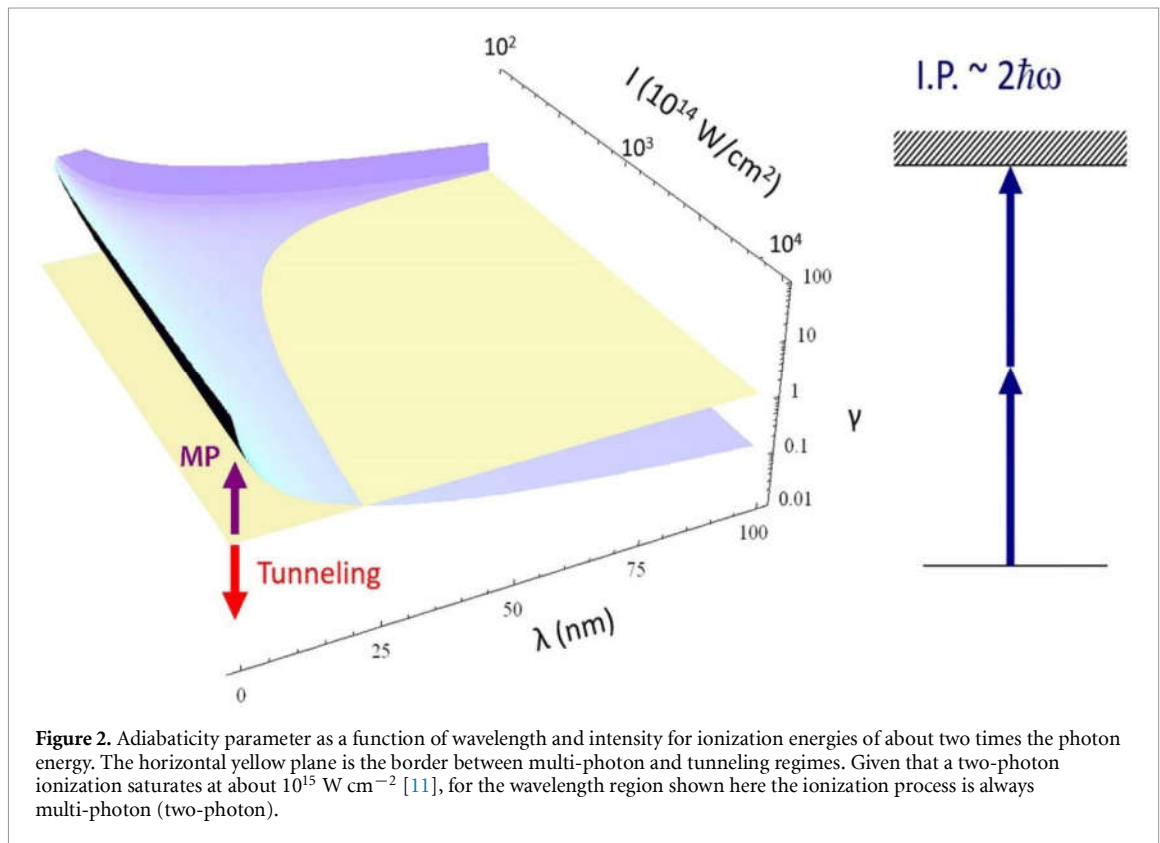
It is worth adding here that the effect of ionization saturation during the raising edge of the radiation pulse is not always a disabling effect. Indeed this effect underlies the temporal gating technique known as 'ionization gating' that enables the generation of isolated attosecond pulses [12, 13].

## 1.2. The ionization of an atom/molecule. 'Coring' vs 'Peeling'

The intricacies of ionization upon interaction of short wavelength radiation with matter are governed by the ratio of the *photon energy* over *ionization energy* of the first inner shell of the matter.

If this ratio is  $> 1$  an inner shell electron is ejected with notably higher probability than an outer one (a process frequently referred to as 'coring') leaving an inner shell hole behind. The hole is eventually filled, in the vast majority of the cases, through an Auger or Coster-Kronig process [14], producing a doubly ionized atom/molecule. Absorption of subsequent photons leads to repetition of the process described, as long as the above mentioned ratio is larger than unity. High charge state ions are thus produced through a sequence of single photon absorption processes (and eventually subsequent relaxation processes), each of which leads to the next charge state of the ion.

The photo-ejection of an inner-shell electron discussed here theoretically can also proceed via MP absorption. However, in order for this process to compete with the ejection of an outer electron, a challenging combination of pulse duration and energy, not available in any laboratory or research infrastructure so far, is required. Thus 'coring' processes are so far sequences of single photon absorption events (sequential coring). In contrast, for a ratio  $< 1$  an outer shell electron is ejected leaving a singly ionized ion behind and absorption of further photons leads to the ejection of additional outer electrons provided that the ejection is energetically allowed (a process frequently referred to as sequential peeling). Under specific conditions, ejection of two electrons leads to a doubly ionized ion without intermediate production



of a singly ionized ion, a process known as direct double (or multiple) ionization. An inner shell non-linear process, i.e. absorption of more than one photons by one or more inner shell electrons leading to some stage of ionization, without formation of intermediate charge states, is currently not possible, since it requires very short pulse durations at high pulse energies, a matter that will be discussed in the next section. Such a process can currently be considered only as a future perspective. On the contrary multi-XUV-photon absorption by outer electrons is feasible at the currently available XUV intensities in FEL infrastructures as well as in laser driven HHG [15, 16] sources. This has led to the revitalization of MP processes, a forefront research topic at optical frequencies in the 70 s, 80 s and 90 s, now in the XUV/x-ray regimes.

### 1.3. The era of non-linear XUV processes, their contribution in attosecond metrology and science

Historically, MP processes trace back to the 30 s. It was Maria Göppert Mayer who first predicted two-photon processes, talking about ‘two quanta jumps’ (Über Elementaraktien mit zwei Quantensprünge”) [17]. About 30 years later, in the 60 s, the invention of the laser led to the first experimental observation of MP processes [18, 19]. Another 30 years later, in the 90 s, the development of intense laser HHG sources [20, 21] led to the first experimental observation of multi-XUV-photon processes [22]. The importance of observable multi-XUV-photon processes relates to a number of advanced applications.

Concerning applications in temporal pulse characterization, non-linear XUV processes hold promise for rigorous attosecond pulse reconstruction. The most frequently used methods for the temporal characterization of fs pulses are based on non-linear processes both in the time domain, like second- and higher-order autocorrelation, frequency resolved optical gating (FROG) [23], attosecond spatial interferometry [24] or in the frequency domain like Spectral Phase Interferometry for the Direct Electric Field Reconstruction (SPIDER) [25] to mention some. In attosecond pulse metrology, due to the lack of sufficient pulse energy, a number of cross-correlation (infrared (IR)/XUV) techniques have been developed such as Reconstruction of Attosecond Beating By Interference of two-photon Transitions (RABBIT) [26], Frequency Resolved Optical Gating for Complete Reconstruction of Attosecond Bursts (FROG-CRAB) [27], Phase Retrieval by Omega Oscillation Filtering [28], *in-situ* [29], atto-clock [30], double-blind holography [31] and the attosecond streaking [32] methods. A summary of these approaches can be found in the perspective article on the attosecond pulse metrology [33]. Non-linear XUV processes allowing the performance of second-order autocorrelation based techniques relying solely on the XUV radiation provide an alternative attosecond pulse characterization approach bypassing possible inconsistencies inherent in the other methods [34]. Still, robust utilization of non-linear XUV processes in attosecond pulse

characterization is subject to the availability of sufficient stability of the XUV radiation parameters and high repetition rate sources.

Applications in the investigation of ultra-fast dynamics using attosecond pulses follow similar pathways. Cross-correlation (IR/XUV) approaches like RABBIT, RAINBOW RABBIT [35] and attosecond streaking have been successfully used in numerous fascinating applications; atomic inner-shell spectroscopy [36], real-time observation of ionization [37], light wave electronics [38] and molecular optical tomography [39, 40] are some examples of such experiments. Other more recent applications of attosecond pulses include ionization delay in solids [41] and atoms [36, 37] and molecules [42, 43], electron dynamics [44], charge migration [45, 46], build-up of a Fano-Beutler resonance [35], ionization dynamics in chiral molecules [47], to mention some from the very many. Alternatively, non-linear XUV processes allow conducting XUV-pump-XUV-probe experiments with sub-fs temporal resolution overcoming complications, that may arise in some cases in conventional IR/XUV pump-probe experiments, related to distortions suffered by the system under investigation due to the IR laser/matter interaction that may obscure the intrinsic dynamics of it [48]. XUV-pump-XUV-probe schemes involve at least two-XUV-photon processes and thus non-linear XUV processes offer an advantageous tool in attosecond metrology.

An additional advanced application of non-linear XUV processes arises from the spatial selectivity they provide. Since the non-linear process becomes observable at high intensities and thus in focused beams, the focal area provides spatial selectivity allowing 3D mapping of a sample. Spatio-temporal resolution (4D) may reach the sub- $\mu\text{m}$  and attosecond regimes.

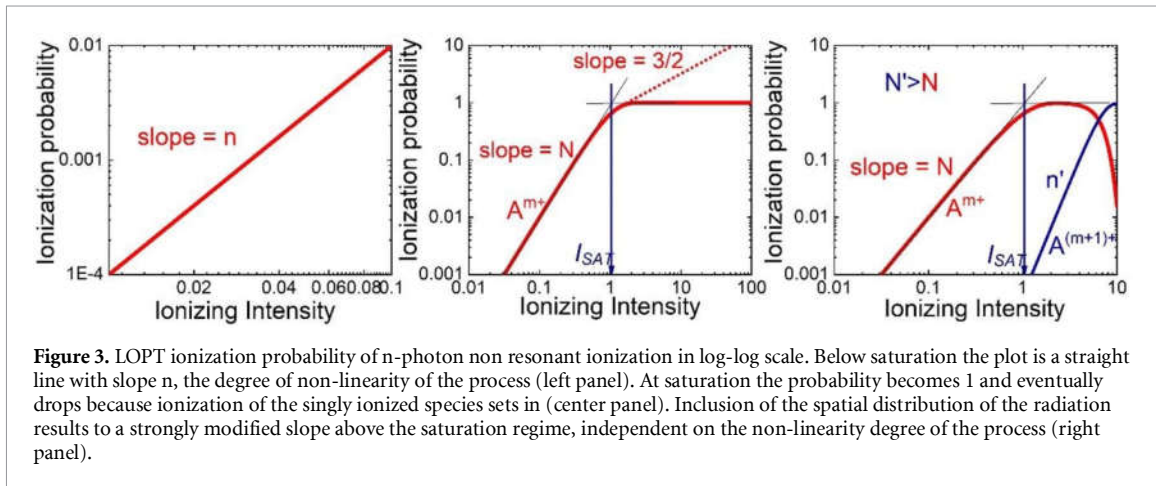
Attosecond pulses as coherent pulses allow frequency domain Ramsey spectroscopy type of measurements [49–51] as well. The superposition of two mutually delayed attosecond pulses result in a modulated broad frequency spectrum. Variation of the delay between the two pulses translates to a variation of the position of the frequency peaks. The distance of two consecutive frequency peaks is inversely proportional to the delay of the two pulses. This allows frequency domain measurements the frequency resolution of which is increased when two-XUV-photon transitions are involved coupling narrow spectral width metastable states.

Nonlinear XUV spectroscopy could also be considered an important tool for the validation of numerical models for the description of electronic correlation in atoms and small molecules. In this research direction, the process of two-photon double ionization represents an ideal benchmark. When confined to the attosecond timescale, the correlated electronic dynamics should be manifested in the relative angular distribution of the photoionized electrons [52]. Such an experiment still represents a formidable technological challenge for nonlinear XUV spectroscopy as it would require the combination of high-intensity XUV pulses, attosecond pulse durations (and control of relative delay between two pulses on a similar timescale) and high-repetition rate sources (for the coincidence characterization of the two-photoelectrons). Even though preliminary, partial experimental data on double ionization of helium and neon were obtained at FLASH [53, 54], there are several characteristics of the process that still need to be investigated.

Non-linear XUV processes made their debut some 20 years ago. Limitations preventing their earlier observation relate to the high intensity they require, while their utilization in applications was hampered since they are inherently absorbed by any material. The latter restriction further prohibits the use of refractive optical elements in the experimental set-ups.

High intensity limitations relate to the low throughput of gas target HHG sources and XUV optical elements, while an additional restriction arises from possible reabsorption of the XUV radiation at the source itself. Limitations on the throughput of gas target HHG sources originate from the depletion of the generation medium, which at a given intensity is fully ionized and no medium emitters remains to generate harmonics. Since HHG relies on the interaction of matter with an IR pulse, even if very high laser pulse energies are available ionization will saturate at the leading edge of the laser pulse once the ionization saturation limit is reached. The emitter will be fully ionized and thus the higher intensities will not be ‘seen’ by the depleted generating medium. Moreover, in the created plasma the index of refraction at a given angular frequency  $\omega$ ,  $n_\omega \approx 1 - \frac{\omega_p^2}{2\omega^2}$  is determined by the plasma frequency  $\omega_p = e\sqrt{\frac{N_e}{m\epsilon_0}}$ , with  $N_e$  the electron’s density and  $\epsilon_0$  the vacuum permittivity. Saturation of ionization will result to a large electron density  $N_e$  leading to negative dispersion that may destroy phase-matching.

Reabsorption of the XUV radiation at the source sets additional limitations in the generation medium length and atomic density. The absorption length in the generation medium is given by  $L_{abs} \approx (\sigma N_a)^{-1}$ , where  $\sigma$  is the absorption cross section and  $N_a$  the atomic density. Therefore, increasing the medium length or the gas pressure such that  $L_{abs} N_a > \sigma$  would be meaningless as reabsorption would prevent an increased throughput. Mitigation strategies of medium depletion and reabsorption are described in section 2.



Other source throughput limitations are raised by the necessity to use only reflection optics in steering, focusing or splitting the XUV beam, because XUV radiation is highly absorbed when it propagates in matter. This point will also be discussed in section 2.

#### 1.4. MP ionization yields and the required XUV intensity and pulse duration parameters

In a  $n$ -photon non-resonant ionization process the time evolution of the ionization probability  $P(t)$  can be described by the rate equation:

$$\frac{dP(t)}{dt} = (1 - P(t)) \sigma^{(n)} F^n(t) \quad (1.4.1)$$

where

$$F^n(t) = \frac{I(t)}{\hbar\omega} = F_0 f(t) \quad (1.4.2)$$

is the photon flux,  $I(t)$  the intensity envelope,  $F_0$  the instantaneous peak photon flux,  $\omega$  the angular frequency,  $f(t)$  the temporal pulse profile with  $f(t=0) = 1$  and  $\sigma^{(n)}$  the generalized  $n$ -photon ionization cross section usually given in  $\text{cm}^{2n} \text{s}^{n-1}$  so that the rate  $dP/dt$  is given in  $\text{s}^{-1}$  when the intensity is given in  $\text{W}/\text{cm}^2$ .

Defining an effective time  $t_{\text{eff}} = \int_{-\infty}^{\infty} f^n(t') dt'$  integration of (equation 1.4.1) yields an ionization probability at the end of the ionizing pulse:

$$P(t \rightarrow \infty) = 1 - \exp\left(-\sigma^{(n)} F_0^n t_{\text{eff}}\right). \quad (1.4.3)$$

Below saturation of ionization, i.e. when  $\sigma^{(n)} F_0^n t_{\text{eff}} \ll 1$

$$\ln P(t \rightarrow \infty) = n \ln F_0 + \ln \sigma^{(n)} + \ln t_{\text{eff}}. \quad (1.4.4)$$

Thus, the ionization probability depends linearly on the photon flux (or intensity) in log-log scale below saturation, with a slope equal to the degree of the non-linearity  $n$  as shown in figure 3 (left panel). Including saturation and defining the ionization saturation intensity as

$$I_{\text{SAT}} = \frac{\hbar\omega}{\sqrt[n]{\sigma^{(n)} t_{\text{eff}}}}, \text{ the ionization probability at the end of the pulse becomes}$$

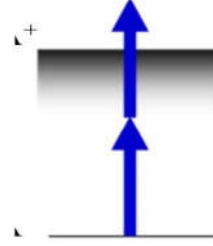
$$P(t \rightarrow \infty) = 1 - e^{-\left(\frac{I}{I_{\text{SAT}}}\right)^n} \quad (1.4.5)$$

and for  $I \ll I_{\text{SAT}}$  reduces to  $P(t \rightarrow \infty) = \left(\frac{I}{I_{\text{SAT}}}\right)^n = \sigma^{(n)} F_0^n t_{\text{eff}}$ . A plot of (equation 1.4.5) in log-log scale is shown in figure 3 (right panel). As  $I$  approaches  $I_{\text{SAT}}$  the increase of the probability slows down and at saturation becomes 1. Above saturation ( $I > I_{\text{SAT}}$ ) the probability drops because the ionization of the singly ionized species sets in.

It should be noted that because the ionization radiation at the focus has a 3D intensity distribution  $I = I(x, y, z)$  the ionization probability will also have a spatial distribution  $P = P(x, y, z)$  and even if the central part of the interaction volume is saturated the surrounding will not be. When the ionization probability

**Table 2.** Typical two-XUV-photon ionization parameters.  $\tau_\omega$  denotes the duration of the XUV pulse.

$\sigma^{(2)}$	$10^{-50} \text{ cm}^4 \text{ s}$
$\hbar\omega$	20 eV
$\tau_\omega$	2 fs
$V_{\text{int}}$	$10^{-7} \text{ cm}^3$
$n_{\text{atom}}$	$2.6 \times 10^{15} \text{ cm}^{-3}$
$I_\omega$	$10^{11} \text{ W cm}^{-2}$
$\eta$	0.5



measurement is not spatially confined, but it is integrated for the entire interaction volume the probability  $P(t \rightarrow \infty) \int \int \int p(x, y, z) dx dy dz = \int \int \int \frac{I(x, y, z)}{I_{\text{SAT}}} dx dy dz$  will neither stabilize at unity nor drop at and above the saturation intensity respectively. It will continue increasing due to the volume integration.

For a Gaussian distribution in cylindrical coordinates the spatiotemporal intensity distribution is

$$I(r, z; t) = I(t) \frac{w_0^2}{w(z)^2} \exp\left[-\frac{2r^2}{w(z)^2}\right] \quad (1.4.6)$$

where  $r$  is the radius,  $z$  is the beam propagation axis and  $w(z)$  is the beam radius, defined in terms of the beam waist  $w_0$  as  $w(z) = w_0 \sqrt{1 + (z/z_R)^2}$ . The ion yields can then be integrated using the expression

$$P(t \rightarrow \infty) = \int_0^{r_{\text{max}}} \int_{z_{\text{min}}}^{z_{\text{max}}} 2\pi r P(r, z) dz dr \quad (1.4.7)$$

where  $P(t \rightarrow \infty)$  is the integrated over the volume ionization probability at the end of the pulse and  $P(r, z)$  the ionization probability at each point  $(r, z)$ . Above saturation, (equation 1.4.7) results to a line with a slope of 3/2 as shown in figure 3 (middle panel). This effect known as the ‘volume effect’ can be eliminated by a spatially confined measurement of the ions as will be discussed in section 2.

The generalized  $n$ -photon ionization cross section in the electric dipole approximation within the LOPT reads:

$$\sigma^{(n)} \propto \left| \frac{\sum_{i_1} \dots \sum_{i_{n-1}} \langle g | \vec{r} \hat{e} | i_1 \rangle \dots \langle i_{n-1} | \vec{r} \hat{e} | f \rangle + \int d\varepsilon \langle g | \vec{r} \hat{e} | \varepsilon \rangle \langle \varepsilon | \vec{r} \hat{e} | f \rangle}{[E_{i_{n-1}} - E_g - (n-1)\hbar\omega] \dots [E_{i_1} - E_g - \hbar\omega]} \right|^2 \quad (1.4.8)$$

where  $|g\rangle$ ,  $|f\rangle$ ,  $|i_k\rangle$  ( $k = 1, \dots, n-1$ ) and  $|\varepsilon\rangle$  are the ground, final, all electric dipole allowed intermediate bound states involved and all electric dipole allowed continuum states involved respectively.  $E_g$ ,  $E_f$ ,  $E_{i_k}$  and  $E$  are the corresponding eigenenergies,  $\vec{r}$  is the electron position operator and  $\hat{e}$  the electric field polarization unity vector. *Ab initio* calculations of  $\sigma^{(n)}$  are feasible for some atoms for which the eigenstate wave functions can be deduced from the Schrödinger equation when exact or accurate atomic potentials are available, as for instance for H and He atoms [55]. In general, generalized ionization cross section can be calculated to some degree of approximation. However, good estimates of  $\sigma^{(n)}$ , sufficient to describe the essential features of the process, can be obtained from the corresponding cross section of Hydrogen atom using scaling laws [56, 57].

Based on the above discussion one can estimate the required XUV intensities in order to achieve observable two-XUV-photon ionization, i.e. the lowest possible non-linear ionization process. The measured number of ions  $N_{\text{Ion}}$  per pulse will be given by

$$N_{\text{Ion}} = P \times V_{\text{int}} \times n_{\text{atom}} \times \eta \quad (1.4.9)$$

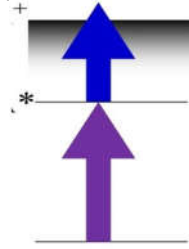
where  $P$  is the ionization probability,  $V_{\text{int}}$  the interaction volume,  $n_{\text{atom}}$  the target atomic (/molecular) density and  $\eta$  the detection efficiency of the measuring device. Typical values of the above quantities are summarized in table 2. These parameters result  $N_{\text{Ion}} = 2-3$  ions/pulse. Thus, intensities of  $10^{11} \text{ W cm}^{-2}$  are at the limits of observable two-XUV-photon ionization. Intensities  $\geq 10^{12} \text{ W cm}^{-2}$  are required for reliable two-XUV-photon ionization intensity dependence experiments.

In large pulse duration interactions ionization yields are enhanced if the process is resonant with one (or more) of the eigenstates. Large pulse duration here means that the duration is comparable or larger than the lifetime of the state, when decaying through spontaneous emission. For a two-photon resonantly enhanced ionization by a bichromatic field the ionization rate becomes

$$P = \int_{-\infty}^{\infty} \sigma_1 \times F_1 dt \times \int_{-\infty}^{\infty} \sigma_2 \times F_2 dt = \sigma_1 \times \sigma_2 \int_{-\infty}^{\infty} \frac{I_1}{\hbar\omega_1} dt \times \int_{-\infty}^{\infty} \frac{I_2}{\hbar\omega_2} dt \quad (1.4.10)$$

**Table 3.** Typical two-XUV-photon resonantly enhanced ionization parameters. Two XUV frequencies are assumed. The first being resonant with the transition frequency from the ground to the excited state and the second one is in general different than the first one.  $\tau_i$  ( $i = 1,2$ ) are the pulse durations of the two XUV frequencies, which are assumed to be equal

$\sigma_1 \times \sigma_2$	$10^{-34} \text{ cm}^4$
$\hbar\omega_{1,2}$	10 eV
$\tau_{1,2}$	2 fs
$V_{int}$	$10^{-7} \text{ cm}^3$
$n_{atom}$	$2.6 \times 10^{15} \text{ cm}^{-3}$
$I_{1,2}$	$10^{11} \text{ W cm}^{-2}$
$\eta$	0.5



with  $\sigma_i$  ( $i = 1,2$ ) being the single photon absorption cross sections of the two steps and  $F_i$ ,  $I_i$ ,  $\omega_i$  the photon fluxes, intensities and angular frequencies of the two fields, respectively. Using typical values for all the quantities (e.g. those of table 3) one can evaluate the number of generated ions per pulse from (equation 1.4.9) to be  $N_{Ion} \approx 2500$  ions/pulse, which is three orders of magnitude larger than in the non-resonant.

In obtaining the above number of ions we used as the effective duration of a Gaussian pulse

$\tau_{eff} = \int_{-\infty}^{\infty} e^{-\left(\frac{t}{2\tau_{1,2}}\right)^2} dt = 3.5\tau_{1,2}$ . However, for the evaluation of the ion yield here, no account is taken that from the broad spectrum of the radiation pulse only the part that corresponds to the state width is resonant and thus only this fraction should be used from the initial intensity ( $10^{11} \text{ W cm}^{-2}$ ).

Ionization by the two parts of the spectrum lying above and below the resonance will cancel due to the opposite detuning and thus to the opposite phases of the corresponding ionization pathways. Taking this into account for bound states with lifetimes of the order of 1 ns, the resonant channel of the ionization becomes negligibly small compared to the non-resonant channel. For this reason, for very short pulses in the attosecond and few fs temporal regime the resonant character of the process is lost unless the lifetime of the state is comparable to the pulse duration as is the case for fast decaying autoionizing states (AIS). In this case the resonant character will be present and may enhance the yield. The situation may become more complex if the experimental parameters become such that the population of the resonant state becomes comparable to the remaining population in the ground state. In such cases the ionization yield may be enhanced. Under such conditions the problem is treated more accurately as described in the following paragraphs and even better if it is solved numerically, since then parameters, such as the width and position of the resonant state, are becoming time dependent.

Rigorously, the problem should be treated through the time dependent Schrödinger equation (TDSE) and not through rate equations. In solving the TDSE for the case of a two-photon ionization it is assumed that the system is initially in the ground state,  $|g\rangle$  (energy  $E_g$ ), subject to a radiation field  $E(t)$  with a central-carrier frequency,  $\omega$ , which is near resonant with an excited state  $|a\rangle$  (energy  $E_a$ ).

The atom can be ionized through two different ionization channels; (a) by absorbing two photons non-resonantly (direct channels) and (b) via the excited state, following the absorption of one-photon and ionization from further photon absorption (sequential channel). However, the atom, once found in the excited state can also be de-excited back to its ground state by photon emission. The photoionization scheme is depicted in figure 4.

The TDSE is solved by first transforming to a slowly-varying-amplitude (SVA) [58] system and then applying the rotating wave approximation (RWA) [58, 59] on the amplitude equations for the ground and the excited state, i.e. eliminating the resulting high frequency terms  $[(E_a - E_g)/\hbar + \omega]$  keeping terms oscillating at  $[(E_a - E_g)/\hbar - \omega]$ . It is worth emphasizing that the change to a system of SVA variables does not involve any approximation and as such the transformed TDSE is still exact in the context of a two-level system interacting with a laser field. The applied transformation effectively extracts the fast-oscillating part of the amplitude coefficients due to the energy difference of the two states  $\sim (E_a - E_g)$  (also known as the interaction picture). The SVA transformation combined with the RWA results in expressing the TDSE in terms exclusively of slowly-varying variables, namely, the field's envelope and the periodic  $\sim \exp(i(E_a - E_g)/\hbar - \omega)t$  factor. The corresponding (strongly-oscillating) term  $\sim [(E_a - E_g)/\hbar + \omega]$  is discarded. This method is effective if i) it can be modeled in factors of an envelope-like amplitude  $E_0(t)$  and a periodic term oscillating with a central carrier frequency e.g.  $\sim E_0(t) \times \cos(\omega_{XUV} \times t)$ ; for the latter assumption a quantitative condition is  $dE_0(t)/dt \ll \omega_{XUV} E_0(t)$ , which generally holds for a few fs pulse with central frequency in the XUV regime and ii) as long as the field is not extremely intense so that  $\Omega_0 \ll \omega_{XUV}$ ,  $\Omega_0$  being the Rabi frequency. The transformed amplitude equations for the ground and the excited state now obey the following coupled-system of differential equations,



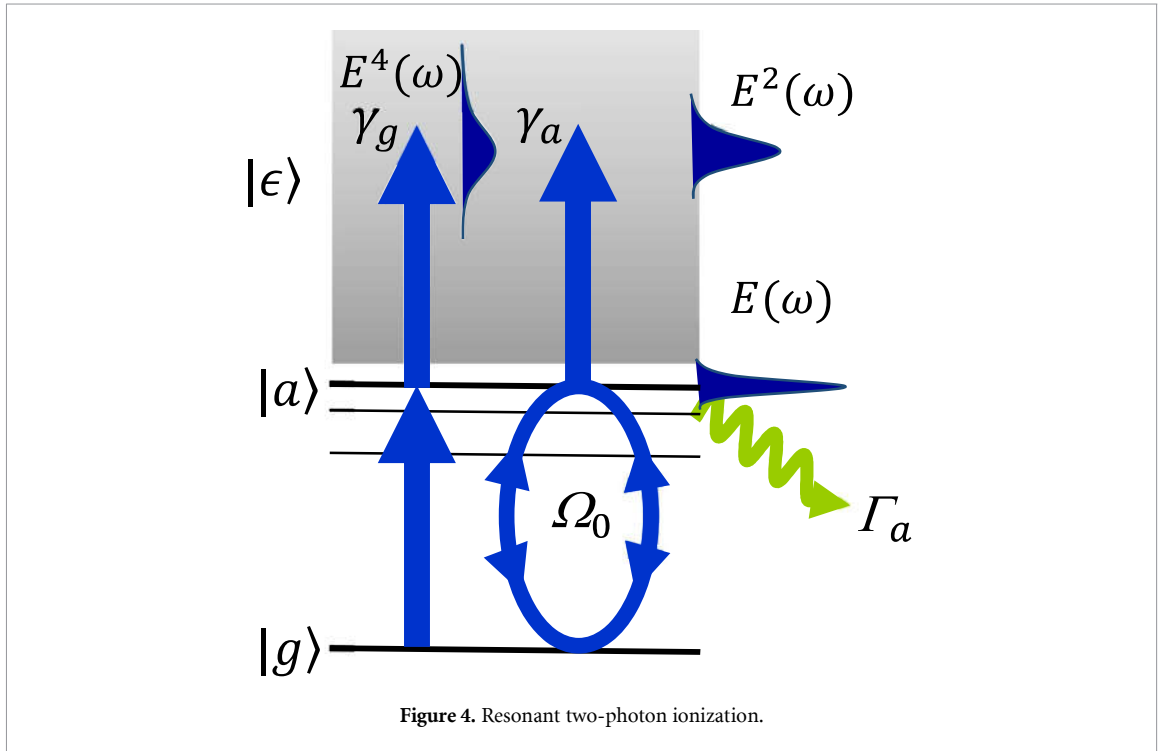


Figure 4. Resonant two-photon ionization.

$$i \begin{bmatrix} \dot{c}_g(t) \\ \dot{c}_a(t) \end{bmatrix} = \begin{bmatrix} \varepsilon_g(t) - \frac{\gamma_g(t)}{2} & \Omega_0 - \frac{i}{2} \\ \Omega_0 - \frac{i}{2} & \varepsilon_a(t) - \frac{\Gamma_a + \gamma_a(t)}{2} \end{bmatrix} \begin{bmatrix} c_g(t) \\ c_a(t) \end{bmatrix} \quad (1.4.11)$$

where  $q = \frac{2\Omega_0}{\sqrt{\gamma_g\gamma_a}}$ ,  $\varepsilon_i(t) = E_i + s_i(t)$ ,  $i = g, a$  and  $c_g(t)$ ,  $c_a(t)$  the time dependent state amplitudes, i.e. the square root of the probability to find the system in the corresponding state at time  $t$ . In these relations  $s_g$ ,  $s_a$  and  $\gamma_g$ ,  $\gamma_a$  are the light shifts, i.e. the shift of the energy of the atom/molecule states induced by the radiation and the widths of the states.  $\Gamma_a$  is the ionization width of the excited state due to other decay channels (e.g. autoionization). Therefore, the dynamic energies  $\varepsilon_g, \varepsilon_a$  have incorporated the ac-Stark shifts; also the  $q$ -parameter describes the interference between the resonant (sequential) and the non-resonant (direct) ionization channels (similar to the traditional  $q$ -Fano parameter). In the above form of the TDSE, all quantities, but  $\Gamma_a$ , are (non-oscillating) time-dependent quantities varying with the field's envelope,

$$s_g(t) = s_g I_0^2 f^4(t), \quad \gamma_g(t) = \gamma_g I_0^2 f^4(t) \quad (1.4.12)$$

$$s_a(t) = s_a I_0^2 f^4(t), \quad \gamma_a(t) = \gamma_a I_0^2 f^4(t) \quad (1.4.13)$$

$$\Omega_0(t) = \Omega_0 f(t), \quad \Omega_0(t) = \frac{1}{2} d_{ga} E_0 f(t) \quad (1.4.14)$$

where  $f(t)$  is the field's normalized envelope and  $I_0 = |E_0|^2/4$ . The above system of equations results in a time-dependent ionization probability:

$$\dot{P}(t) = |\sqrt{\gamma_g} C_g + \sqrt{\gamma_a} C_a|^2 \quad (1.4.15)$$

(in density matrix notation  $\gamma_g \rho_{gg} + \gamma_a \rho_{aa} + 2\sqrt{\gamma_g\gamma_a} \text{Re}(\rho_{ga})$ , the diagonal matrix elements of  $\rho_{gg}, \rho_{aa}$  being the state amplitudes, i.e. the square root of the population of the states  $g$  and  $a$  respectively, and the non-diagonal matrix element  $\rho_{ga}$  being the so called coherence that relates to the induced dipole moment).

Note that for the ac-Stark shifts, in the range of intensities where the RWA is applicable, the following inequalities apply:  $s_g \ll \varepsilon_g$  and  $s_a \ll \varepsilon_a$ . The reason for this resides in the structure of  $s_g$  and  $s_a$  quantities; the numerator is positive while the denominator is positive up to a certain value and then becomes negative, thus amounting to a reduced value due to mutual cancellations.

#### Solutions for the amplitudes.

In the general case the TDSE system should be solved numerically, especially in the case where all involved parameters are of comparable magnitude i.e. detuning, decay widths, Rabi frequency. Nevertheless, an

approximate analytical expression for the state amplitudes and the ionization is possible for a many cycle field; the general solution for the amplitudes takes a very simple form, as a linear combination of exponentials:

$$c_g(t) = \frac{e^{i\hat{\delta}t/2}}{\hat{\Omega}} \left[ \hat{\Omega} \hat{s}_+(t) - \hat{\Delta} \hat{s}_-(t) \right] \quad (1.4.16)$$

$$c_a(t) = \frac{\hat{\Omega}_0}{\hat{\Omega}} e^{i\hat{\delta}t/2} \hat{s}_-(t) \quad (1.4.17)$$

where all the quantities with hats are complex numbers and determined by the generalized Rabi-frequency, the effective ionization widths and the dynamic detunings,

$$\hat{s}_{\pm} = \frac{1}{2} \left( e^{i\hat{\Omega}t/2} \pm e^{-i\hat{\Omega}t/2} \right), \quad \hat{\Omega} = \sqrt{\hat{\delta}^2 + 4\hat{\Omega}_0^2} \quad (1.4.18)$$

$$\Gamma = \gamma_a + \Gamma_a + \gamma_g, \quad \gamma = \gamma_a + \Gamma_a - \gamma_g \quad (1.4.19)$$

$$\hat{\Delta} = \delta + i\frac{\Gamma}{2}, \quad \hat{\delta} = \delta + i\frac{\gamma}{2} \quad (1.4.20)$$

$$\hat{\Omega}_0 = \Omega_0 \left( 1 - \frac{i}{q} \right) \quad (1.4.21)$$

$$\delta = \varepsilon_g + \omega - \varepsilon_a. \quad (1.4.22)$$

In the general case where  $\Gamma_a$  is present, ionization may be calculated by,

$$P(t) = 1 - |C_g(T)|^2 - |C_a(T)|^2 e^{-\Gamma_a(t-T)} \quad (1.4.23)$$

where  $T$  is the interaction time (e.g. the pulse duration). The expression when only photoionization is present is calculated to be,

$$P(t) = 1 - e^{-\Gamma t/2} \left[ |\hat{s}_+|^2 + \frac{\hat{\Delta}^2 + |\hat{\Omega}_0|^2}{|\hat{\Omega}|^2} |\hat{s}_-|^2 + 2\text{Re} \left\{ \frac{\hat{\delta}^* \hat{\Omega}}{|\hat{\Omega}|^2} \hat{s}_+ \hat{s}_- \right\} \right]. \quad (1.4.24)$$

In all the cases below one can check the role of the interaction time (pulse duration),  $T$ , in the observed yields in addition to the role of the ionization width  $\gamma$ , Rabi-frequency,  $\Omega_0$ , and the detuning  $\delta$ .

### 1.5. Resonant case $\delta \simeq 0$ and no direct-channel ( $\gamma_g = 0$ ) (strong-field)

In this case all quantities become real and the expression for the amplitudes take a very simple oscillatory form. Since,

$$\Gamma = \gamma_a = \gamma, \quad 1/q = 0, \quad \Omega = \sqrt{4\Omega_0^2 - (\gamma/2)^2} \quad (1.4.25)$$

assuming the strong-field case where  $4\Omega_0^2 > (\gamma/2)^2$  one easily can arrive to the expressions,

$$c_g(t) = \frac{2\Omega_0}{\Omega} e^{-\Gamma t/4} \sin\left(\frac{\Omega t}{2} + \varphi\right) \quad (1.4.26)$$

$$c_a(t) = i \frac{2\Omega_0}{\Omega} e^{-\Gamma t/4} \sin\left(\frac{\Omega t}{2}\right) \quad (1.4.27)$$

with the phase-lag  $\varphi$  defined as,  $\tan\varphi = \frac{2\Omega}{\gamma}$  ( $\cos\varphi = \frac{\gamma}{4\Omega_0}$  and  $\sin\varphi = \frac{\Omega}{2\Omega_0}$ ). Note that the phase-lag between the ground and the excited state is determined by the ratio  $\frac{\gamma}{\Omega_0}$ . In this case the ionization probability is given by,

$$P(t) = 1 - \frac{4\Omega_0^2}{\Omega^2} e^{-\gamma t/2} \left[ 1 - \frac{\gamma}{4\Omega_0} \cos(\Omega t - \varphi) \right]. \quad (1.4.28)$$

Therefore, the ionization probability is purely oscillatory with a period determined by the generalized Rabi frequency. In the ‘weak’-field case ( $4\Omega_0^2 < (\gamma/2)^2$ ) the results are obtained if one sets  $\Omega \rightarrow i\Omega$ , and the oscillatory functions become purely exponential.

### 1.6. Strong and short pulse ( $\gamma, \Gamma \ll \Omega_0$ and $\gamma T, \Gamma T \ll 1$ )

In this case where both the direct- and the sequential channels are present the following expression for the ionization rate can be derived,

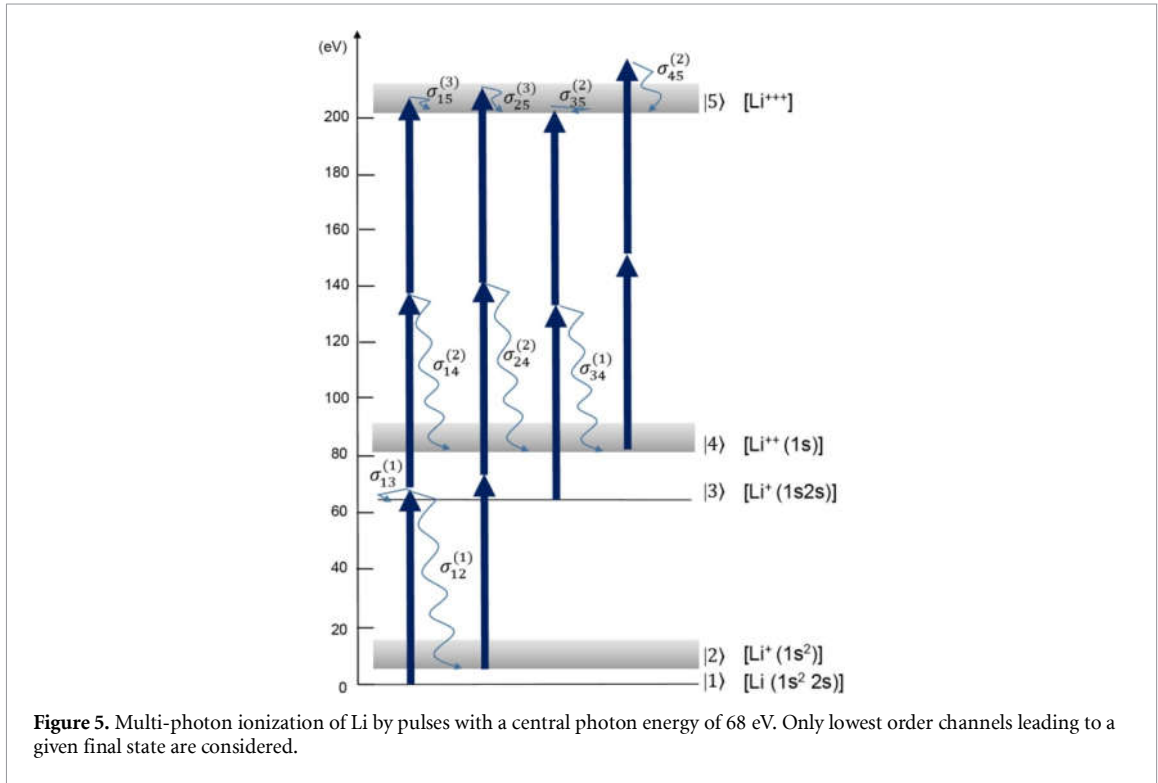
$$\dot{P}(t) \cong \gamma_a \frac{4\Omega_0^2}{\delta^2 + 4\Omega_0^2} \sin^2 \Omega t + \gamma_g + 2q\gamma_a\gamma_g \frac{\delta}{\delta^2 + \Omega_0^2} \sin^2 \Omega t. \quad (1.4.29)$$

If the interaction time is much larger than the Rabi’s period ( $|\Omega|t \gg 1$ ) then integration of the above time-dependent ionization probability provides an ‘average’ ionization rate, which resembles a Fano-profile placed on a constant background (of the direct ionization channel).

### 1.7. MP multiple ionization

When the intensity is sufficiently high multiple ionization may occur involving i) sequential processes where all intermediate charge states get populated and the next charge state is reached through photon absorption by the previous populated charge states, ii) direct processes in which two or more electrons are ejected without formation of the lower charge states and iii) processes populating excited bound or AIS of the ionic stages. Thus, different channels can contribute to the formation of a certain charge state. The temporal evolution of the processes involved can be described through rate equations from which the ionization probability can be evaluated.

At this point, it should be made clear that the most general treatment of the ionization processes should involve the density matrix formulation for all possible states of the combined atom and laser system with both the coherent (relative atomic amplitude’s phases are important) and incoherent processes incorporated on an equal footing. Additionally, the density matrix is a statistical approach appropriate not only for pure states but also for mixed states, i.e. ensembles of which we only know their statistical distribution. In this sense the TDSE and the rate equations have a different validity range of parameters, in fact they are placed on opposite sides. When the relative atomic phases are unimportant then one can obtain a simplified model of the ionization process, that of rate equations. In the opposite case, i.e. the case when the relative atomic phases cannot be ignored, the TDSE formulation can be used in order to describe an ionization process; thus it represents the other ‘simplified’ extreme (treating only pure states and only partially decoherence phenomena) where the relative phases are crucial for the system’s dynamics. However, for the latter case TDSE is only nominally a simplified system of ‘equations-of-motion’ since all the excited (bound and continuum) atomic states in principle should be included. Nevertheless, a simpler form can be obtained under certain conditions involving amplitude equations, of the same type as discussed in the two-level system model earlier. In all of its full generality, the TDSE system can be solved very accurately only for the lighter atomic systems, such as the hydrogen and helium. For all other atomic systems more drastic approximation models are used, especially when multiphoton processes contribute to the excitation and ionization. One may loosely say that the rate equations treat the ionization process in an ‘averaged’ fashion thus ignoring any phase relationship between the atomic states (bound or excited). The state’s population are the main actors in this model. The SVA and the RWA are applied into the TDSE with the additional assumption that the relative phases follow adiabatically the populations of the atomic states. Eventually, the ionization process is described by a single absorption rate, via the (multiphoton) ionization cross section. Therefore, any resonance features are only implicitly incorporated in the values of the cross section for the given field’s frequency. This particular approximation gradually loses its meaning as the spectrum of the field broadens (or equivalently the pulse shortens) since the cross sections are, in principle, meaningful quantities only for monochromatic pulses. Hence, one may not hope to fully replicate the results either of a model based on a full density-matrix or TDSE formulation but only to estimate ionization rates for experimental schemes which meet the physical conditions set above. The resulting rate equations have the structure of a system of ordinary differential equations which normally may be calculated without complications. This is the task of the rate equations model as it, very nicely, factorizes the ionization process into its main



constituents: the states' population,  $N_i$ , the field part via its flux  $F(t)$  and their interaction strength through the various cross-sections  $\sigma_{ab}$ . The formidable task is the calculation of the cross sections rather than solving the rate equations. The structure of the rate equations is such that the total rate of the system sums to zero as one should expect from a population-transfer modeling, a model which in other fields is not the exception but the rule e.g. in biology, chemistry, statistics etc. Computationally, the rate equations' approach is by far the less demanding one, followed by the TDSE. The reader interested in a more extensive account of the rate equations ionization model could find it in the classic text by Shore [60].

To give an example of a simple system, assume ionization of Li atoms by a pulse of 1fs duration with central photon energy 68 eV and a peak intensity of  $10^{15}$  W cm $^{-2}$ . The equations of motion for the Li charge states following ionization from the ground state by a pulse with central frequency at 68 eV are given below:

$$Li(1s^2 2s) \frac{dN_1}{dt} = - \left[ \left( \sigma_{12}^{(1)} + \sigma_{13}^{(1)} \right) F(t) + \sigma_{14}^{(2)} F^2(t) + \sigma_{15}^{(3)} F^3(t) \right] N_1 \quad (1.4.30)$$

$$Li^+(1s^2) \frac{dN_2}{dt} = \sigma_{12}^{(1)} F(t) N_1 - \left[ \sigma_{24}^{(2)} F^2(t) + \sigma_{25}^{(3)} F^3(t) \right] N_2 \quad (1.4.31)$$

$$Li^+(1s 2s) \frac{dN_3}{dt} = \sigma_{13}^{(1)} F(t) N_1 - \sigma_{34}^{(1)} F(t) N_3 \quad (1.4.32)$$

$$Li^{2+}(1s) \frac{dN_4}{dt} = \sigma_{14}^{(2)} F^2(t) N_1 - \sigma_{45}^{(2)} F^2(t) N_4 + \sigma_{24}^{(2)} F^2(t) N_2 \quad (1.4.33)$$

$$Li^{3+} \frac{dN_5}{dt} = \sigma_{25}^{(3)} F^3(t) N_2 + \sigma_{45}^{(2)} F^2(t) N_4 + \sigma_{15}^{(3)} F^3(t) N_1 \quad (1.4.34)$$

where  $F(t) = I(t)/\hbar\omega$  is the field's flux and  $\sigma_{ij}^{(n)}$  the generalized cross sections for the respective ionization processes. The order of the cross sections is denoted in parenthesis and is equal to the flux's appearance power. The various pathways are depicted in figure 5 while the ionization yields for the given pulse are plotted in figure 6.

It should be noted that, although the channel to the  $Li^+(1s 2p)$  continuum is energetically open through electron-electron correlation, it is much weaker ( $\sim 15$  times weaker than the channel to  $Li^+(1s 2s)$ ) and thus has been neglected. Also, the two-photon ejection of two electrons from the  $Li^+ 1s 2s$  state (transition  $|3\rangle \rightarrow |5\rangle$ ) has been neglected because this channel is open to only a small part of the bandwidth of the radiation.

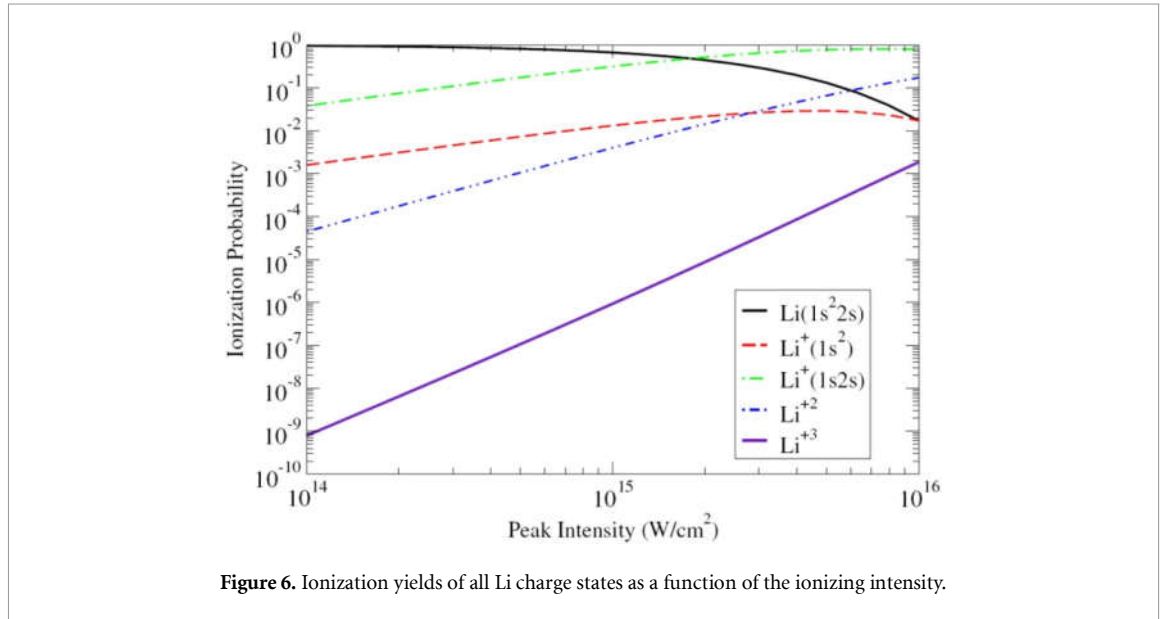


Figure 6. Ionization yields of all Li charge states as a function of the ionizing intensity.

The field's intensity is modelled by  $I(t) = I_0 e^{-(t/\tau)^2}$ , where  $\tau$  is related to the effective pulse duration. The main difficulty in solving the above system of rate equations resides in the calculation of the atomic parameters  $\sigma_{ij}$  since generally several of them have not been yet calculated with a rigorous calculation method. These are then estimated based on scaling properties of atomic systems as well as properties related to the nature of the electromagnetic field interaction. In the present case the following values have been chosen for the calculation of the ionization yields:  $\sigma_{12}^{(1)} = 10^{-19} \text{ cm}^2$ ;  $\sigma_{13}^{(1)} = 2 \cdot 10^{-18} \text{ cm}^2$ ,  $\sigma_{14}^{(2)} = 10^{-53} \text{ cm}^4 \text{ s}$ ;  $\sigma_{24}^{(2)} = 10^{-51} \text{ cm}^4 \text{ s}$ ;  $\sigma_{35}^{(2)} = 10^{-53} \text{ cm}^4 \text{ s}$ ;  $\sigma_{34}^{(1)} = 10^{-19} \text{ cm}^2$ ;  $\sigma_{45}^{(2)} = 10^{-53} \text{ cm}^4 \text{ s}$ ;  $\sigma_{25}^{(3)} = 10^{-87} \text{ cm}^6 \text{ s}^2$  and  $\sigma_{15}^{(3)} = 10^{-87} \text{ cm}^6 \text{ s}^2$ .

As it is beyond the scope of the present work to describe the calculation details we delegate the interested reader to other more elaborate works for this task [61, 62] (and references therein). A package for the *ab-initio* calculation of one- and two-photon cross sections of two-electron atoms, using a configuration interaction (CI) B-splines method can be found in [63]. There is a large number of publications involving rate equations of two- (or few-) photon ionization. The 'simplest' case is He for which a study in the photon energy range 45–54 eV can be found in e.g. [64]. In case of more complex systems and more photon ionization cases the number of rate equations increases significantly [65].

There are many publicly available packages for numerical calculations in atomic and molecular systems such as, the COWAN package [66], BSR [67], BSPCI2E [63], QPROP [68], RMT [67], and the quantum chemistry packages UKRmol [69] and MOLPRO, to mention a few; but, due to the highly specialized numerical approaches, the codes are mostly developed and used in-house.

The above discussion and parameters concern multi-XUV-photon absorption by an outer shell electron, which are processes that have been realized utilizing initially individual harmonics of laser radiation and later on radiation of FEL sources, as well as laser based attosecond-pulse sources. Apart from sequences of single photon inner-shell absorption processes leading to multiple ionization, two- or more XUV photon absorption by an inner-shell electron has not been demonstrated yet. This is attributed mainly to the lack of the required experimental parameters that would allow such a process to compete with lower linear processes of the outer shell electrons. In order to estimate such experimental parameters, cross sections of two- (or multi-) photon inner-shell ionization are required. Good estimates of two-photon K-shell cross-sections can be calculated for hydrogen-like ions using scaling. For a two-photon ionization (equation 1.4.8) reads

$$\sigma^{(2)} \propto \omega^2 \left| \frac{\sum_{\nu_1} \langle g | \vec{r} \hat{e} | \nu_1 \rangle \langle \nu_1 | \vec{r} \hat{e} | f \rangle + \int d\epsilon \langle g | \vec{r} \hat{e} | \epsilon \rangle \langle \epsilon | \vec{r} \hat{e} | f \rangle}{E_L - E_g - \hbar\omega} \right|^2. \quad (1.4.36)$$

Continuum renormalization  $\langle \epsilon | \epsilon' \rangle = \delta(E - E')$  results in  $|f\rangle$ ,  $|\epsilon\rangle \propto Z^{-1}$ ,  $Z$  being the charge of the nucleus of the hydrogen-like ion. Thus, the matrix elements and  $d\epsilon$  in (1.4.36) scale with  $Z$  like:

$$\langle g | r | i \rangle \propto Z^{-1}, \langle i | r | f \rangle \propto Z^{-2}, \langle g | r | \epsilon \rangle \propto Z^{-2}, \langle \epsilon | r | f \rangle \propto Z^{-3} \quad (1.4.37)$$

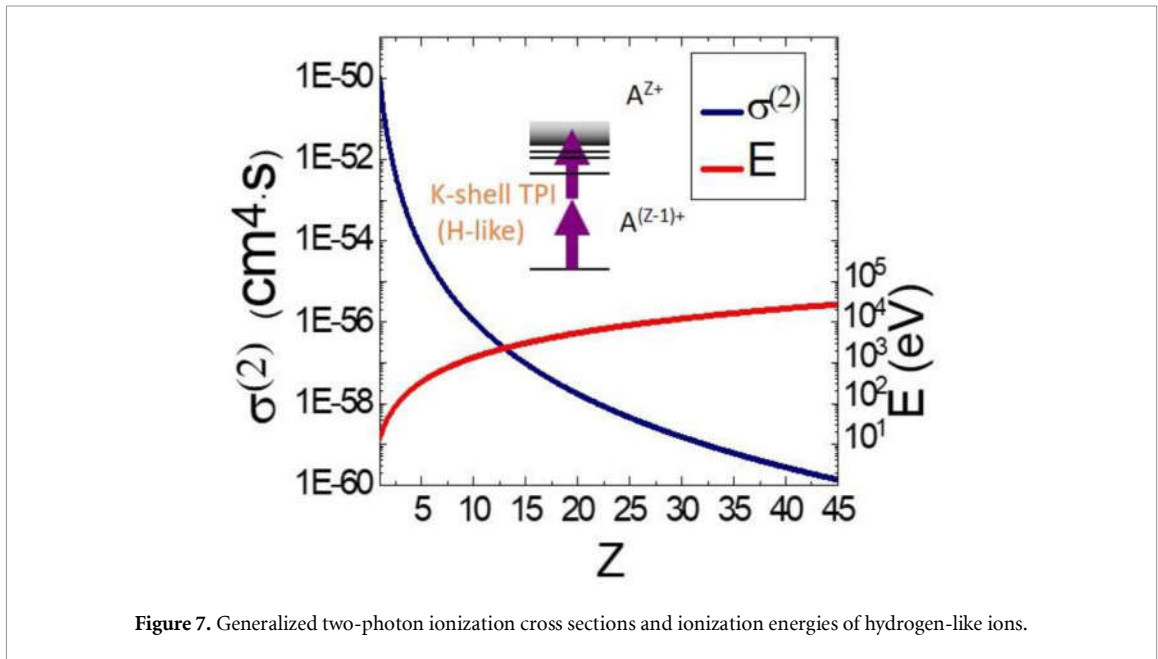


Figure 7. Generalized two-photon ionization cross sections and ionization energies of hydrogen-like ions.

and

$$d\epsilon \propto Z^2. \quad (1.4.38)$$

Hence, the cross section

$$\sigma^{(2)}(Z, \omega) = \frac{1}{Z^6} \sigma^{(2)}\left(Z=1, \frac{\omega}{Z^2}\right) \quad (1.4.39)$$

drops dramatically for heavier ions.

Figure 7 shows the  $Z$  dependence of a two-photon K-shell ionization generalized cross section of hydrogen-like ions and the corresponding photon energy threshold at which the two-photon ionization channel opens. Due to the  $Z^{-6}$  dependence of the cross section, in order for the two-photon ionization process of the inner shell to compete with the single photon ionization of the outer shell at intensities lower than the ionization saturation intensity, the pulse duration has to be extremely short. To give an example, for  $Z = 4$  (beryllium atom) and photon energy 110 eV, approximating the two-photon K-shell ionization of the atom with that of the hydrogen-like ion of the same  $Z$ , the two photon generalized cross section becomes  $\sigma^{(2)}_{\text{K}} = 5 \cdot 10^{-54} \text{ cm}^4 \cdot \text{s}$ . The L-shell single photon ionization cross section is  $\sigma^{(1)}_{\text{L}} \sim 10^{-20} \text{ cm}^2$ . For a pulse duration of 40 asec the two-photon K-shell ionization will become the dominant process at intensities larger than  $5 \cdot 10^{16} \text{ W cm}^{-2}$ , while ionization saturation occurs at  $\sim 10^{18} \text{ W cm}^{-2}$ . Therefore, for a large interval of intensities, ionization will essentially occur via two-photon K-shell absorption.

For a pulse duration of 1 fs, two-photon K-shell ionization becomes comparable to the L-shell single photon ionization just before saturation sets in. It becomes obvious that energetic attosecond pulses are required in order for the process to become observable. For the time being, even for the relative low  $Z$  of our example, the parameters discussed are not available in any currently operational XUV source. Nevertheless, they are close to become available in the near future. However, when going to higher  $Z$  the parameters become extreme. To give an example, for neon intensities of the order of  $10^{20} \text{ W cm}^{-2}$  and pulse durations of the order of 10 asec, are necessary.

It is worth noting that (equation 1.4.1) is rigorously valid only if the field is fully coherent i.e. if its quantum state is the coherent state of light. For any quantum state of light, the ionization probability rate is

$$\frac{dP(t)}{dt} \propto \sigma^{(n)} G^{(n)} \quad (1.4.40)$$

where  $G^{(n)}$  is the  $n$ -th order intensity correlation function of the field. For the coherent state of light  $G^{(n)} \cong \langle N \rangle^n$ ,  $N$  being the photon number and thus (1.4.40) reduces to 1.4. For the chaotic state of light (thermal light)  $G^{(n)} \cong n! \langle N \rangle^n$ , and for a photon number squeezed state of light  $G^{(n)} \cong (2n-1)!! \langle N \rangle^n$  [70–72]. Thus, at first glance and kind of counterintuitively MP ionization by chaotic light is more efficient than by coherent light. However, if one realizes that in chaotic light, the photons are statistically more

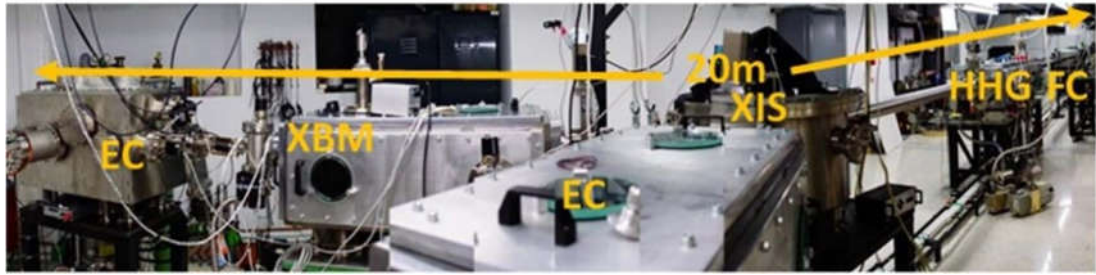


**Figure 8.** The 20GW HHG beamline of the attosecond science and technology lab of FORTH. EC: Experimental chamber; XBM: XUV Beam Manipulation chamber; XIS: XUV-IR separation chamber; HHG: High Harmonic Generation chamber; FC: Focusing Optics chamber.

'bunched' than those of a coherent light, this observation is of no surprise. This is experimentally verified already in the 70's [73] and recently in a more controllable way [74]. This dependence of the efficiency of MP processes on the quantum state of the light may lead to differences in experiments conducted at FELs and XUV sources based on the process of HHG by lasers [11].

## 2. Experimental methods for non-linear XUV optics

As stated in the introductory section we address mainly laser-driven tabletop XUV sources. In this section we focus on methods and instrumentation dedicated to the investigation of non-linear XUV processes exploiting such sources. Several of the methods and instrumentation coincides with those used in FEL infrastructures. Methods and instrumentation that are exclusively used in FEL facilities are beyond the scope of this manuscript and thus will not be addressed here.

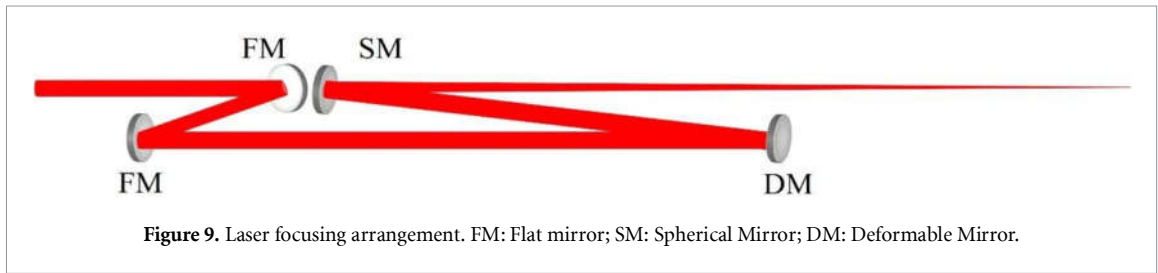
### 2.1. High photon-flux laser driven, tabletop XUV sources based on harmonic generation in gas targets

Laser-driven attosecond sources are based on HHG ([20, 21] and references therein). Harmonic generation is a highly non-linear process and consequently its throughput is drastically increased with the driving intensity and more precisely with the order of non-linearity, which is between 4 and 5 [75–77]. As mentioned in section 1.3, the main obstacles in reaching the high XUV photon fluxes, required for inducing non-linear XUV processes in laser based attosecond sources using gas targets as non-linear media are the depletion of the generating medium, the phase mismatch due to plasma formation and the XUV radiation reabsorption by the generating medium itself. Partial mitigation of these limitations, leading to a higher source throughput, is to drive the harmonic generation process using long focal length optical elements to focus the laser in the medium. In this way the cross section of the laser beam in the interaction region increases and thus a higher number of emitters and photons contribute to the generation while ionization remains below saturation.

When a small length medium in comparison to the confocal parameter is used, as is the case when pulsed nozzles are employed, the interaction length remains effectively unchanged when the focal length is increased. When a large length medium, as compared to the confocal parameter is used, as is the case when long cells are used, increasing the focal length will increase the interaction length and the product  $L_{abs}N_a$  will become larger than  $\sigma$ . Reabsorption will then prevail. In this case the gas pressure must be decreased such that the product will remain smaller than  $\sigma$ . A detailed investigation of the scaling of the source parameters focal length, laser field and atomic density can be found in [78].

An implementation of large focal length (9 m) gas jet source is the 20 GW XUV beamline of the Attosecond Science and Technology lab of the Foundation for Research and Technology, Hellas (FORTH) (figure 8). Using Xe as harmonic generating medium a maximum XUV pulse energy of the order of 200  $\mu$ J in the spectral region 15–30 eV has been demonstrated [11]; more recently a train of pulses with sub-fs pulse durations have been measured [79]. The longest focal length used so far is 17 m at the Max Planck Institute for Quantum Optics. In this beamline using Ne as harmonic generating medium, despite its three orders of magnitude lower conversion efficiency than Xe [80], 40 nJ pulse energies have been achieved in the spectral region 60–130 eV [81].

A similar to FORTH's but more advanced beamline is currently under commissioning at the Extreme Light Infrastructure-Attosecond Light Pulse Source (ELI-ALPS) research infrastructure currently operating at 10 Hz and soon to be operational at 1 kHz repetition rate. Due to the shorter pulse duration of the laser systems at ELI-ALPS a slightly higher pulse energy due to the slightly higher ionization saturation intensity and a significantly higher power is expected. In the same infrastructure a much longer beamline (50 m focal



length) with a series of 15 long gas cells of individually controllable low gas pressure is also under implementation [82].

Due to the relative high IR peak power and short pulse duration used, the focusing of the laser beam occurs through reflective optics. Spherical mirrors of large focal length are a common focusing element. In order to avoid astigmatism introduced by the spherical surface, as small as possible incidence angle has to be used. The phase front of the IR beam in the HHG region can be further improved using of a Deformable Mirror (DM). While a DM is not available in the FORTH beamline, it is used in the ELI-ALPS beamlines. Correcting astigmatism and spatial phase modulations of the IR carrier frequency is important because it improves: i) the focusability of the IR beam and ii) the spatiotemporal properties of the XUV pulses that in turn affect the focusability and pulse duration of the XUV radiation and consequently its intensity. Here spatiotemporal properties refer to spatial wave-front distortions and thus to the overall (non-local) duration of the XUV pulses. A commonly used optical set-up is shown in figure 9. Two parallel flat mirrors introduce a parallel shift of the laser beam such that it bypasses the focusing element steering the beam towards a third flat mirror positioned at furthest long distance possible that reflects the beam towards a focusing spherical mirror at an appropriately small angle of incidence. The long distance between the third flat mirror and the rest of the mirrors is important in order to maintain astigmatism as low as possible. In this arrangement the outgoing beam is propagating in the same direction as the incoming one. In order to achieve best focusability of the laser, its wave-front is often corrected using DMs [83], either in order to directly focus the laser or in combination with another focusing arrangement. DMs allow also varying the position of the focus.

A related approach in improving focusability is to use Bessel-Gauss laser beams that are essentially diffractionless, as demonstrated by Altucci *et al* [84]. Nevertheless, in that work pulses with durations of the order of 100 fs and energies of the order of 100  $\mu$ J were used that allowed the use of diffractive optics in forming the Bessel-Gauss beams. For the parameters of the ELI-ALPS (<7 fs, > 100 mJ) relevant laser system lots of development is required toward the formation of such beams with uncertain outcome.

## 2.2. High photon-flux laser driven, tabletop XUV sources based on harmonic generation in laser-surface plasma

An alternate mitigation measure against the limiting factors in reaching high photon fluxes is the exploitation of non-depleting non-linear media. Such a medium is the laser induced surface plasma and the XUV generating process is high harmonic generation emission by this plasma. Due to the non-depleting non-linear medium, laser fields well in the relativistic regime can be used. During laser-matter interaction the electrons of charge  $q$  are driven by the Lorentz force applied by the electric  $E$  and magnetic  $B$  field of the radiation according to

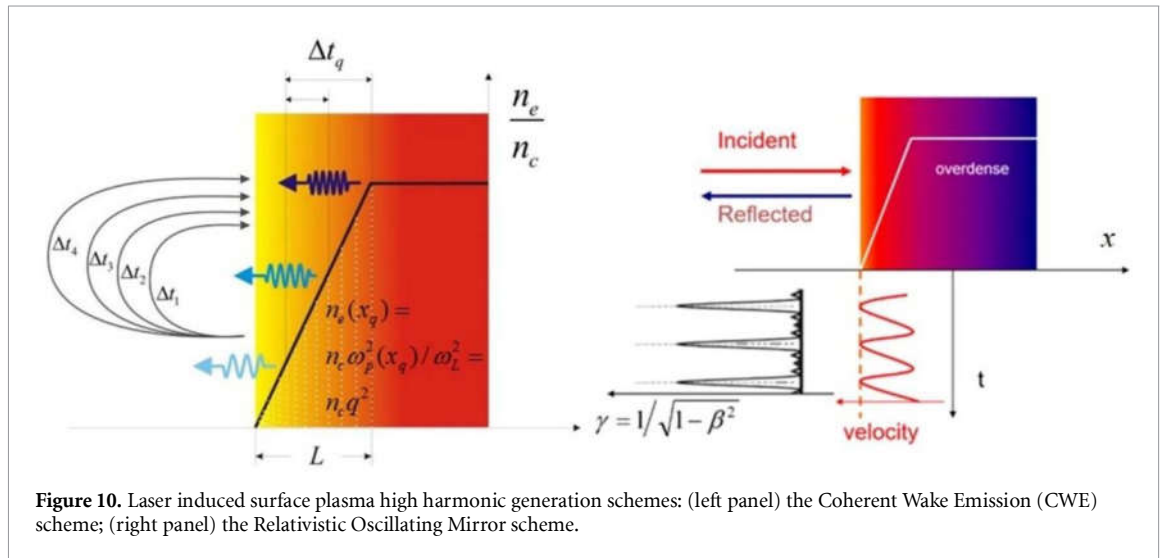
$$\vec{F} = q \left( \vec{E} + \left( \frac{\vec{v}}{c} \wedge \vec{B} \right) \right). \quad (2.1)$$

If the velocity of the electrons  $v$  remains much smaller than the velocity of light  $c$  ( $v \ll c$ ), the magnetic term can be neglected and the electron motion in a linearly polarized field reduces to a harmonic oscillation. For velocities comparable with the light velocity, the action of the magnetic term sets in, introducing a force component along the light propagation direction within the plasma, resulting into a negative-positive charge separation underlying laser particle acceleration and harmonic generation processes. A quantity defined by the wavelength  $\lambda$  and the field amplitude  $E_0$  or the vector potential  $A_0$  that distinguishes between relativistic and non-relativistic interactions is the so-called normalized vector potential

$$\alpha_L = \frac{eA_0}{mc^2} = \frac{eE_0\lambda}{mc^2}. \quad (2.2)$$

For  $\alpha_L < 1$  the interaction is non-relativistic, while for  $\alpha_L > 1$  is essentially relativistic. For a driving laser with central wavelength  $\lambda = 800$  nm  $\alpha_L$  becomes unity for an intensity of the order of  $10^{18}$  W cm $^{-2}$ . Thus, at this

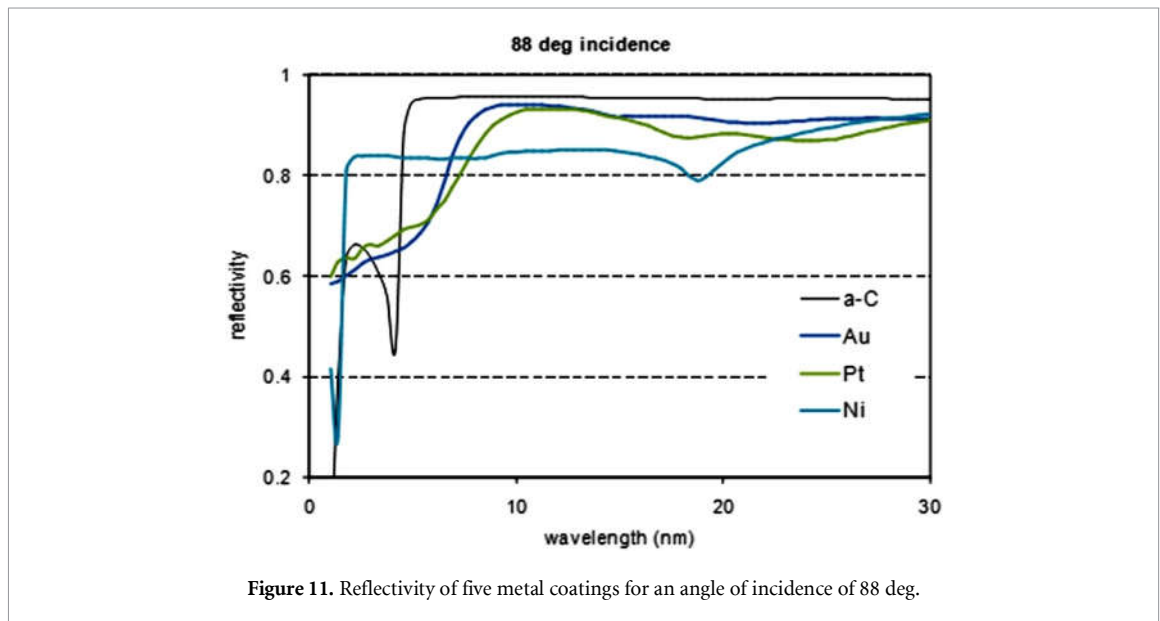




wavelength, the relativistic regime is reached for intensities higher than  $10^{18} \text{ W cm}^{-2}$ . However, for longer wavelengths, i.e. wavelength in the mid-IR or far-IR spectral region, the relativistic regime is reached as much lower intensities. E.g. at  $\lambda = 12 \mu\text{m}$   $\alpha_L$  becomes unity already at intensities  $\sim 5 \cdot 10^{15} \text{ W cm}^{-2}$ , which introduces a new area of applications of new intense mid-IR and far-IR laser sources.

In the sub-relativistic regime the harmonics are produced through the so called Coherent Wake Emission process [85, 86] (figure 10, left panel). Electrons emerging from the plasma gradient are accelerated in the vacuum driven by the field, and upon sign reversal of the field are returned to the plasma exciting a plasma wave that due to the multi-cycle driving field emits harmonics. The emitted frequency is the plasma frequency  $\omega_p(x_q)$ ,  $x$  being the axis perpendicular to the surface, and the index  $q$  denotes the corresponding harmonic.  $\omega_p(x_q)$  relates to the plasma electron density and the harmonic order as  $n_e(x_q) = n_c \frac{\omega_p^2(x_q)}{\omega_L^2} = n_c q^2$ ,  $n_c$  being the critical plasma density. Hence the emitted radiation has a spectral chirp and the shorter the emitted wavelength the deeper point in the plasma it is emitted from [87]. When the solid density is reached no shorter wavelengths can be emitted and thus the harmonic spectrum depicts a cut-off. Due to the different time the electrons spend in the vacuum when emitting different wavelengths, the emitted XUV radiation has a temporal chirp.

As  $\alpha_L$  increases beyond 1 the relativistic interaction effects start to play a more dominant role [88]. The laser drives an overdense plasma such that there is charge separation. The electrons are moving under the interaction with the E and B fields of the laser as well as under the restoring force. Ions are considered to remain essentially at rest due to their much larger than the electron mass. The resulting motion is a non-harmonic periodic motion of the electron-vacuum interface that reaches in short time intervals velocities close to the velocity of light. This motion generates the so called  $\gamma$  spikes,  $\gamma$  being the Lorentz factor  $\gamma = \sqrt{\frac{1}{1-\beta^2}} = \sqrt{\frac{1}{1-v^2/c^2}}$  (figure 10, right panel). The incoming laser radiation is reflected by the fast moving plasma surface and thus its wavelength is Doppler shifted by the generating  $\gamma$  spikes towards very short wavelengths. The processes often referred to as Relativistic Oscillating Mirror have been extensively studied both theoretically and experimentally [2, 86, 89–93]. Through laser surface plasma harmonic generation emission of keV photons [94], XUV pulse energies at the source of  $40 \mu\text{J}$  [95], and sub-fs duration XUV pulse trains have been reported [96]. The collective nature of the plasma medium, the diversity of the laser-plasma parameter space, and a variety of potential geometrical irradiation configurations give rise to a large degree of freedom in tuning the generation process from high harmonic XUV [97, 98] down to the THz [99] domain. This also necessitates appropriate control of the interaction in order to achieve optimal HHG conditions, setting state of the art technological demands [100]. The main of those are high laser peak power, high laser peak to background contrast, elimination of unwanted laser pre-pulses, demanding ‘cleaning’ procedures of the laser pulse through additional plasma mirrors, control of the plasma density gradient [101], micrometer accurate positioning of the tight focus on the target, sensitive alignment of the tightly focusing element commonly an off axis parabola and debris management. An optimal implementation rests on developing a robust method that efficiently balances all these sensitive parameters. Laser surface plasma harmonic generation holds the promise of delivering unprecedented pulse energies of short wavelength radiation with ultra-short pulse duration [102] and has also been proposed as a potential candidate in achieving super high intensities [103, 104] for probing vacuum quantum electrodynamic effects with



currently available lasers. Nonetheless, gas target HHG sources, based on well-established and less challenging technologies, have for the time being more advanced operational parameters such as pulse energies and pulse durations compared to current laser surface plasma harmonic generation sources.

### 2.3. XUV optical elements for high photon-flux laser driven, XUV/attosecond sources

The photon flux and power that reaches the area where the XUV radiation interacts with the system under investigation in an experimental attosecond beamline is notably reduced due to reflections from the steering optics in the beamline.

Obviously only reflective optical elements can be used as refractive materials absorb the XUV radiation. For low XUV photon energies 10–30 eV close to normal incidence metal (commonly Au) coated optics can be used supporting the large bandwidth of the XUV radiation. Normal incidence, which in many cases is more convenient to use, is also possible exploiting multilayer mirrors. The drawback in this case is that the more broadband a multilayer mirror is, the higher the losses it introduces. For the spectral regions not covered by multilayer mirrors and/or ultra-broadband optics, grazing incidence geometries and metal coated reflectors are used. Figure 11 shows the wavelength reflectivity dependence of several metal coatings for an 88° angle of incidence. Reflectivity of the order of 90% is feasible using grazing incidence geometries. Nevertheless, positioning and alignment of optical elements at grazing incidence is a highly sensitive and tedious procedure.

From the optics' field point of view, a further challenge when HHG sources are used to induce non-linear XUV processes is the separation of the unwanted IR laser beam from the XUV radiation. Thin filters transmitting the XUV and absorbing the IR cannot be directly used because they would be destroyed by the strong IR radiation. They can only be used for selection of the desired spectral region and for blocking any residual IR radiation, after the IR photon flux has been substantially reduced. The reduction of the flux can be achieved by the use of Si plates.

A Si surface placed at the Brewster angle of the p-polarized IR beam (75° for radiation of 800 nm) strongly absorbs the IR field and efficiently reflects the XUV radiation. Figure 12 depicts the reflectivity of 800 nm and 50 nm radiation as a function of incidence angle for s and p polarizations. At 75° there is a strong suppression of the IR while the reflectivity of the XUV exceeds 90%.

For high average power IR laser sources [82] absorption of the IR may modify the surface due to thermal effects. In this case IR transmitting materials, like grazing incidence multilayer based antireflections coatings can be used. Such elements can also provide XUV reflectivity > 70% at photon energies > 40 eV.

Another IR suppression approach is the use of annular driving laser beams. Due to the non-linearity of the HHG process, at specific phase-matching conditions, the XUV propagates with smaller divergence than the IR radiation. Driving the non-linear medium with an annular beam formed using a circular beam stop at the center of the IR beam, one can achieve that, after the generation of the harmonics, the XUV beam propagates in a small angle cone, while the IR propagation is essentially outside this cone and thus can be blocked using an aperture. The XUV propagates through the aperture, while the IR is stopped by it. Any residual IR radiation inside the XUV beam can now be absorbed by thin metal filters that also select the XUV

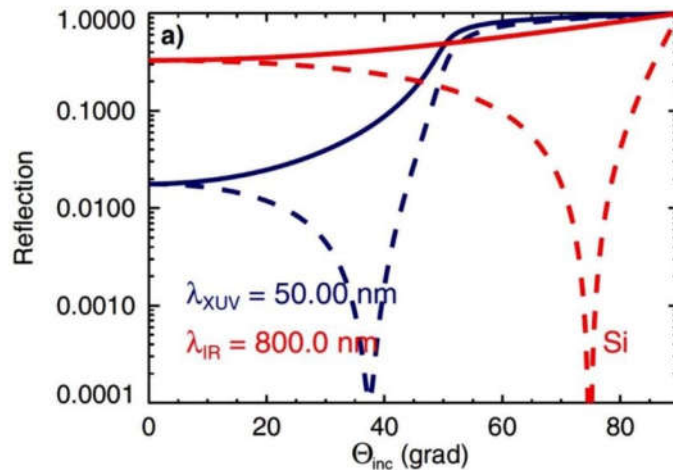


**Figure 12.** Reflectivity of Si as a function of angle of incidence for radiation of 800 and 50 nm. The dash line is the reflectivity of the p-polarization and the solid line that of the s-polarization.

spectral region of interest. Annular beams are also very useful when the IR radiation is not exclusively p-polarized, as is the case when polarization gating is used [105, 106].

In reaching high XUV intensities tight focusing of the XUV radiation is required. Close to normal incidence spherical mirrors, metal coated or multilayer whenever satisfying the requirements of the experiment is the most convenient approach. When spherical reflecting surfaces cannot be used because of large losses in photon number or low quality focal areas, reflection at grazing incidence on focusing surfaces other than spherical is the alternative that is commonly used. Ellipsoidal surfaces [107] are able to focus to the smallest focal spots positioning the XUV source in the one of the ellipse focus and obtaining the XUV focus at the second focus of the ellipse. Since in this case grazing incidence is needed, large ellipsoidal surfaces have to be used with high surface flatness which is a technological challenge. Moreover, aligning the ellipsoidal such that minimal focal spots are reached is a tedious procedure. An approximation of the ellipsoidal surface is a toroidal one which is a very common focusing surface employed in the XUV spectral region [108]. Today set-ups consisting of two toroidal mirrors are commercially available. The first mirror focuses and the second one corrects focusing errors [109]. Another optical arrangement that is used in XUV and x-ray radiation laboratories is the so called Kirkpatrick-Baez (KB) [110] mirror arrangement that uses two focusing surfaces (often spherical ones) where one is focusing horizontally and the other vertically. KB systems are of variable focal length by varying the distance between the two focusing elements [111].

#### 2.4. Attosecond delay lines and non-linear autocorrelators

The absence of refractive optics suitable for the XUV spectral region (due to the immediate absorption of XUV radiation upon propagation in any material), introduces a challenge in time domain applications of non-linear XUV processes like in non-linear autocorrelation (AC) measurements and studies of ultra-fast dynamics. XUV delay-lines cannot use Michelson interferometers, as commonly used in the IR, visible, and x-ray spectral regions, owing to the lack of appropriate transmission-reflection beam-splitters. An XUV Michelson interferometer proposed and demonstrated in the UV uses a diffraction grating as the beam splitter. The principle of the interferometer/delay-line is shown in figure 13. The XUV beam is split in two different diffraction orders (0,1), the diffracted beams are reflected by XUV mirrors and are recombined at the grating through diffraction in the appropriate orders (1,0). Modeling of such a spectrometer has demonstrated dispersionless operation in the attosecond regime [112]. Using such an interferometer a second order AC measurement of UV pulses was performed [113] demonstrating the applicability of the device. In these works, the grating considered or used was a transmission grating. Transmission gratings offer the advantage of having a flat spectral response up to the wavelengths where their material becomes transparent. However, they have the drawback of low diffraction power, which, in the case of double diffraction, as in figure 11, results in a 1% throughput. At the photon fluxes of attosecond XUV beam-lines available today, such a throughput hardly allows the observation of non-linear XUV processes. Furthermore, XUV transmission gratings have to be free standing gratings and they cannot be easily fabricated; moreover, they are sensitive to high average power.

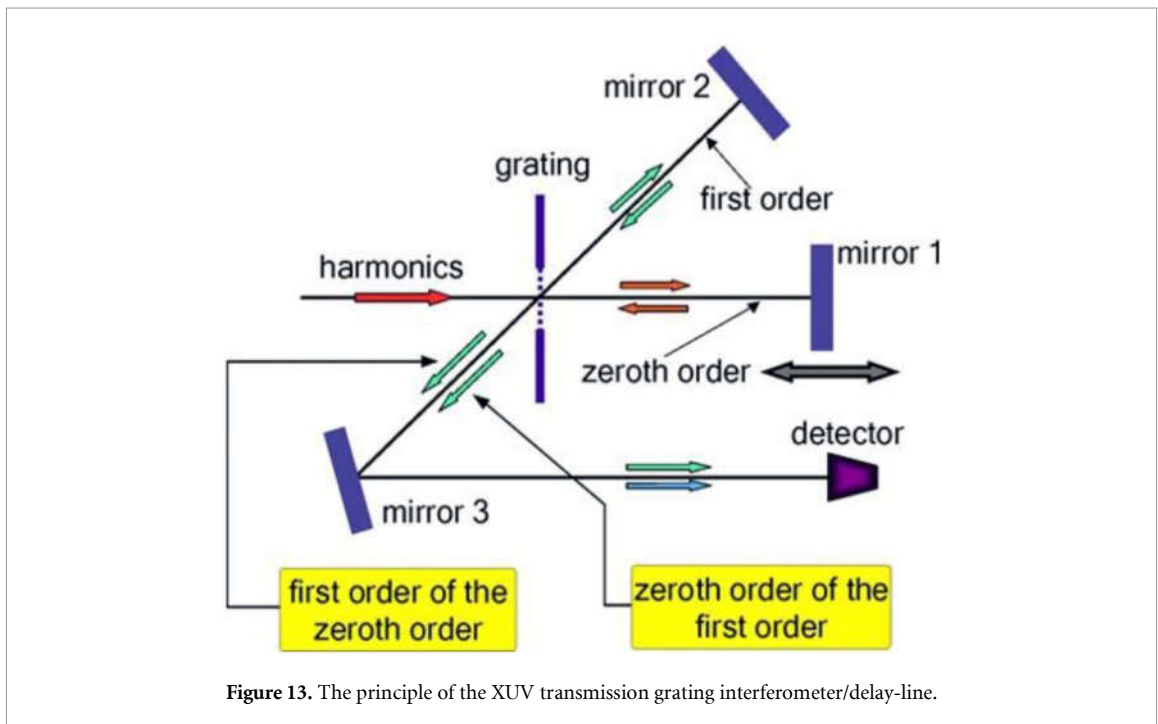


Figure 13. The principle of the XUV transmission grating interferometer/delay-line.

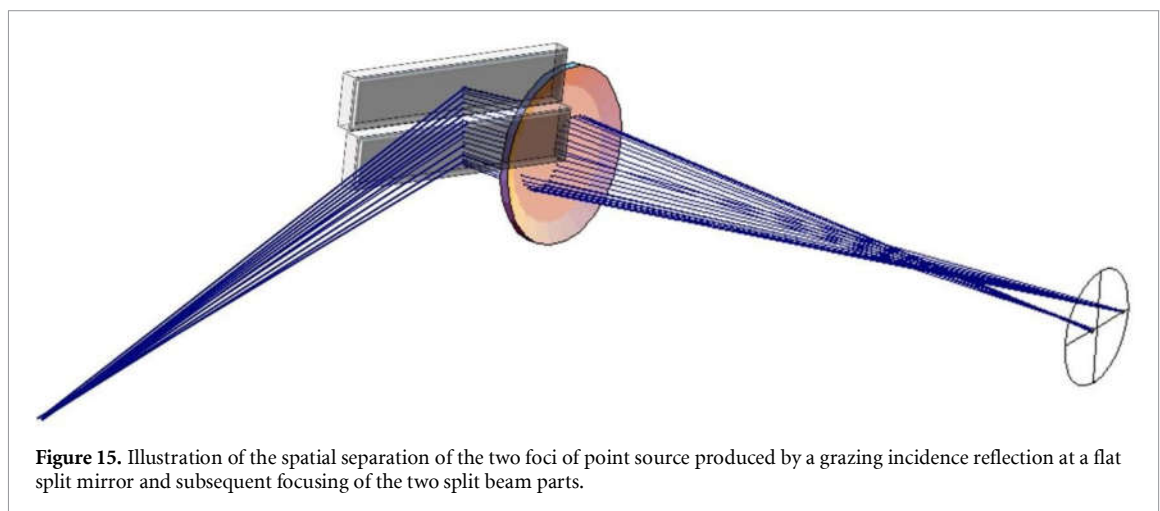
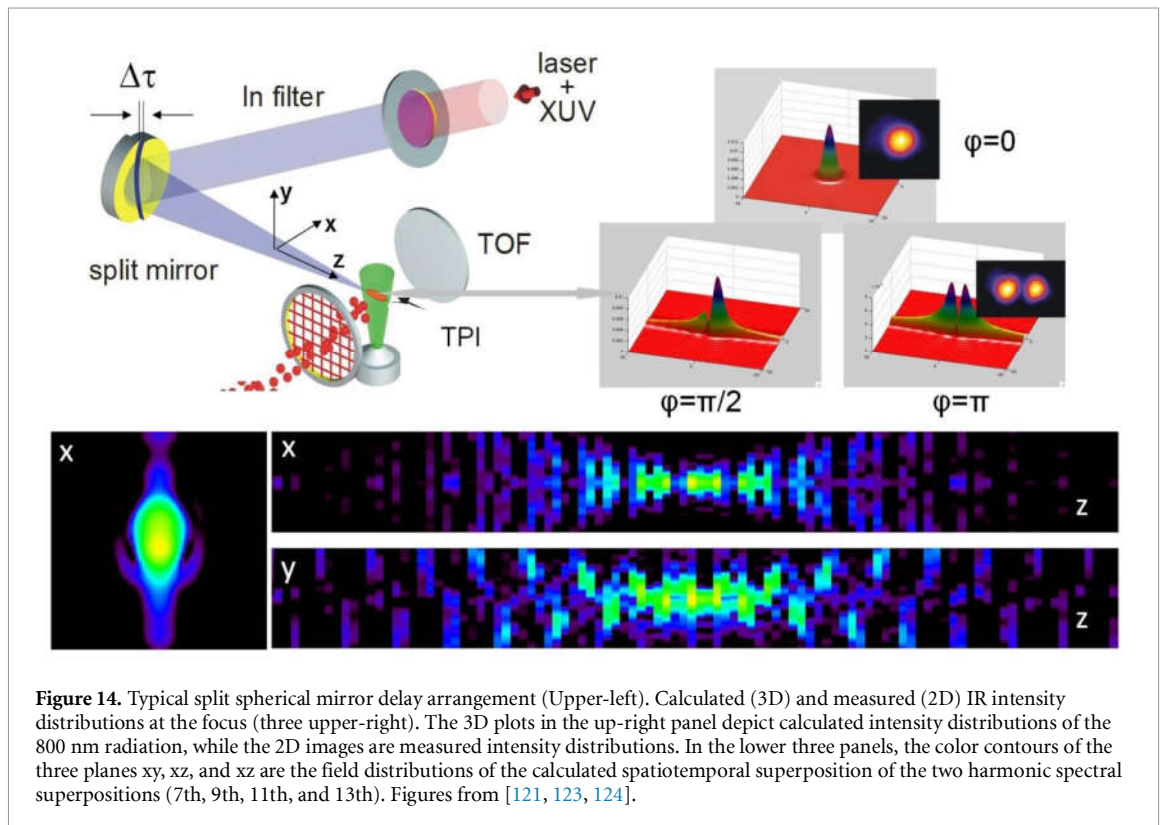
Using XUV reflection gratings substantially higher throughputs may be achieved [114], but the diffraction power becomes wavelength dependent affecting the bandwidth and thus the duration of the XUV pulses. Nevertheless XUV reflection gratings are successfully used in time compensation XUV monochromators [115–119].

The most frequently used set-ups in introducing XUV/attosecond pulse delays are split reflective optical elements [120], one part of which is translated with nm accuracy through piezoelectric translation stages. The split and delay device is not an interferometer as it does not have two arms between which the energy is oscillating with the delay. It is a wave front divider, splitting the beam in two halves, with the one half being delayed in time with respect to the other with attosecond accuracy through the piezoelectric translation. Assuming cylindrical symmetry of the impinging XUV beam the reflected parts are considered to be close to identical. Unless there is spatial selection of part of the out-coming beam, this device cannot produce a first order interferogram by varying the delay. This is because, and in order for energy to be conserved, the spatially integrated out-going beam remains constant due to the lack of second arm. Nevertheless if the two overlapping parts of the beam are inducing a second or higher order process, the yield of this process is delay dependent and thus can be used for the temporal characterization of the XUV pulses [121] as well as in XUV-pump-XUV-probe experiments [106, 122]. Different types of split-delay set ups are used today. In some of them the split optical element is a spherical mirror that produces the two mutually delayed pulses and at the same time focuses the XUV radiation in the interaction area of the study.

Incidence to split spherical mirrors has to be close to normal for keeping astigmatism as low as possible. Metal coated split spherical mirrors can be used for photon energies  $< 30$  eV. Multilayer spherical mirrors are also available for specific spectral regions with the limitations of reflecting power for broadband XUV radiation discussed in section 2.2. A representative set-up of such a spherical mirror split and delay unit is shown in figure 14 (upper left panel). A thin metal filter selects the XUV spectral region, the XUV radiation is then impinging on the split spherical mirrors at effectively normal incidence and is subsequently focused in a gas jet that is ionized and the ionization products are measured with a Time of Flight (TOF) spectrometer. The intensity distribution at the focus of the fundamental wavelength (800 nm) for different delays, corresponding to a phase difference between the two pulses of  $0$ ,  $\pi/2$  and  $\pi$ , is shown in figure 14 (upper right panels).

The field distribution of a superposition of harmonics, produced by the spatiotemporal overlap of the two XUV parts at the focus for a delay of  $T_L/4$  (bottom panel of figure 14), is shown in the lower color contour panels, with  $T_L$  being the period of the IR laser. Alternatively, split flat reflectors are used at grazing incidence and an additional optical element or optical system is used also at grazing incidence for focusing.

A limiting factor, when split optical elements are used, is the spatial separation (introduced by the translation of one of the two mirror parts) of the two foci in the overlapping region. This separation may lead to a non-negligible departure from the spatial overlap of the two beams that would distort the results of



the measurement. For close to normal incidence on split spherical mirrors, the delay induced displacement of the two parts of the mirror, does not affect the results for delays up to 200 fs [123]. Thus, such geometries can be safely used, without corrections, in measuring from attosecond to few hundreds of fs dynamics and/or pulse durations. The situation changes drastically when using grazing incidence geometries. Even small delays may introduce a spatial separation of the two foci.

The effect is illustrated in figure 15 for a flat split mirror in a grazing incidence geometry. It has been shown [108] that for a specific focusing arrangement, delays of tens of fs may introduce a spatial separation of the two foci larger than the focal spot itself and thus corrective actions are required. Such a problem can be solved by means of an optical feedback system [109].

The above described split and delay devices cover the entire VUV-XUV spectral regions. Apart from the above discussed set-ups a Mach-Zender type of split and delay device has been developed and used at FLASH [125]. Proposals for single shot non-linear split and delay devices can be found in the literature [126]

## 2.5. Diagnostics and detection systems

Prerequisites in achieving sufficiently high XUV intensities for non-linear XUV applications that have been addressed in the previous sections are high pulse energy, short pulse duration and XUV radiation with minimum wave-front distortions. The pulse duration in the above described high XUV power beamlines is measured through the 2nd order intensity volume autocorrelation technique (2nd IVAC) [121] utilizing the split spherical mirror delay line described in the previous section and two-XUV-photon ionization as non-linear process detecting the resulting ions as a function of the delay. Due to the high XUV intensities available in these beamlines the 2nd IVAC technique could be used instead of RABBITT based temporal characterization approaches used in low intensity sources. The pulse energy in [11] was measured using calibrated XUV photodiodes that are commonly used in XUV pulse energy determination.

Alternatively, a method to measure on-line the intensity of the XUV pulse uses a gas ionization detector [127, 128], i.e. an absolutely calibrated detector based on photoionization of noble gases at a low target density and detecting photoions and photoelectrons. The number of electrons/ions generated is proportional to the number of photons, to the target density, to the photoionization cross-section and to the length of the interaction volume. Some advantages of this method are: 1) it is almost transparent to the beam and does not alter the beam properties and thus ideal for on-line measurements; 2) it has a wide dynamic range; 3) it is independent from the beam position; and 4) it can be absolutely calibrated with  $\approx 10\%$  accuracy.

In determining the XUV intensity at its focus, where the non-linear XUV processes are studied, the XUV beam waist dimensions are needed. Realistic dimensions can be estimated assuming Gaussian distributions. An advanced direct method for measuring the XUV intensity distribution at its focal area is based on an ion imaging device, known as ion microscope, which measures spatially resolved ion distributions with a spatial resolution of  $1\ \mu\text{m}$ . If the ions are produced through single-photon ionization, the measured spatial ion distribution is identical to the XUV spatial distribution due to the linearity of the ionization process. This device that essentially measures 2D spatial distributions of different ionic charge states with variable magnification is extensively presented in [129–131]. XUV intensity beam profiles are measured either by an XUV beam profiler [11] or through the knife edge technique. The focusability of the XUV beam however depends on the wavefront of the XUV beam. Recently a single shot XUV Hartmann sensor has been developed and used in wavefront measurements of high-order harmonics [132].

In addition to the diagnostics of the XUV beam that are addressed in the previous paragraph, alternative methods in detecting the products of the non-linear XUV processes will be summarized in this section. The so far deduced products are ions in different charge stages [11, 111, 133]. The non-linearity of the process is usually deduced from the slope of the dependence of the ion yield on the XUV intensity (in log-log scale) or by measuring photoelectron spectra [134]. The former is achieved by varying the energy of the XUV radiation in the HHG area. When measuring the ion yield dependence as a function of the XUV intensity, the generalized MP ionization cross sections can be extracted from the ionization saturation intensities (see section 1.4) without knowledge of the atomic density in the interaction area. However, due to the volume effect (section 1.4) the determination of the saturation intensity becomes ambiguous, particularly in two-photon ionization processes where the expected slope of 2 is not easily distinguishable from the slope of  $3/2$  appearing due to the volume effect after saturation. This obstacle can be overcome by measuring spatially resolved ion yields from confined areas in which the radiation intensity is effectively constant.

In the 90's 3D confinement of the area from which ions were detected was achieved through a "four grid reflectron Time of Flight ion mass spectrometer (TOF) [135–137]. The principle of such a measurement is illustrated in figure 16. The blue cube depicts the confined volume for which ions are measured. 2D confinement is realized through an aperture of the second electrode in the ion extraction area of the TOF. Confinement in the third dimension (along the acceleration axis of the ions) is through the four-grid-reflectron. Ions that are exiting the extraction area, are passing through the central hole of the MCP detector (MCPs detector with a central hole) and enter the four-grid-reflectron configuration. The voltage between the second and the third grid in the four-grid-reflectron arrangement gives an additional acceleration to the ions entering the area between these two electrodes. Ions generated on the right of the blue cube area see lower voltage and are less accelerated, thus are reflected between the 1st and 2nd grid of the reflectron (red-trajectory). Ions generated on the left of the blue cube are experiencing the highest acceleration and thus penetrate through all four grids (blue trajectory).

Ions produced within the confined area (blue cube) are passing through the first, second and third grid and are reflected between the third and the fourth ones getting an additional acceleration between grid 2 and 3, i.e. are reaching the MCP detector at earlier times than those produced on the right of the blue cube (green trajectory). The mass peak is split into two corresponding to the two groups of ions. If the volume of the cube is sufficiently small, ionization in it can be fully saturated free of volume effects. This is illustrated in the mass spectra shown in the lower panel of figure 16 and measured at two different intensities. The 'fast' peak

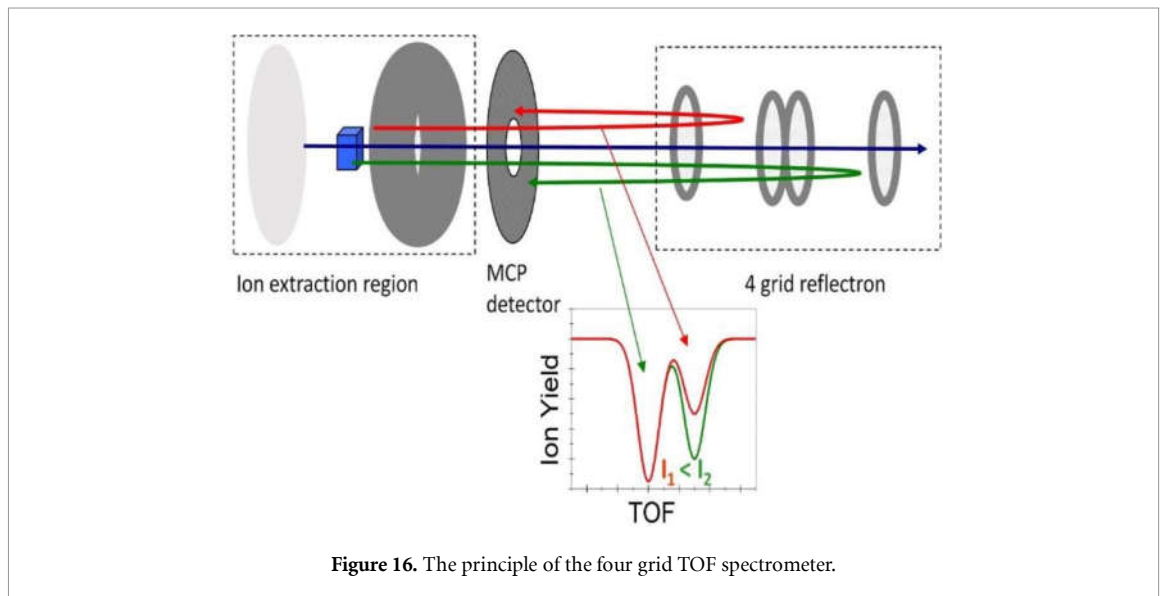


**Figure 16.** The principle of the four grid TOF spectrometer.

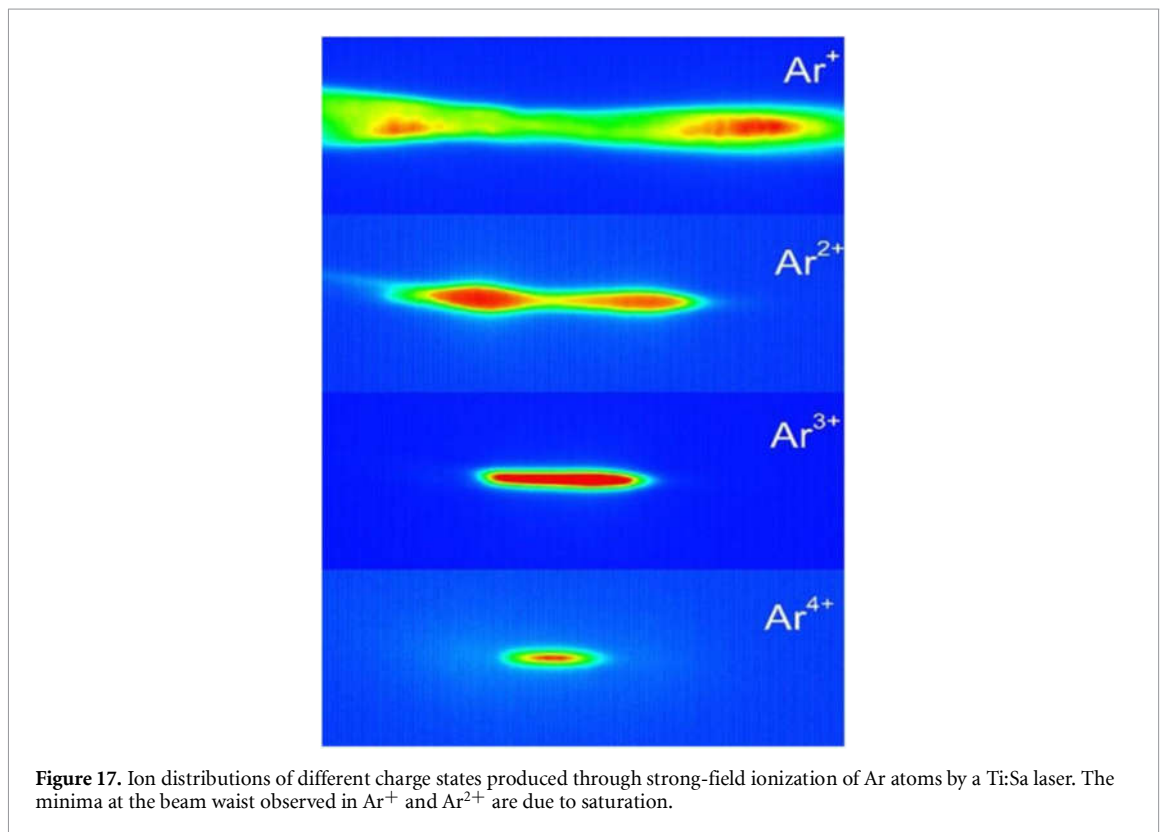


**Figure 17.** Ion distributions of different charge states produced through strong-field ionization of Ar atoms by a Ti:Sa laser. The minima at the beam waist observed in  $Ar^+$  and  $Ar^{2+}$  are due to saturation.

has the same height at both intensities because of saturation, while the ‘slow’ one increases at the higher intensity ( $I_2$ ) due to volume effects.

An advanced version of measuring volume-effect-free MP ionization is using the previously mentioned ion microscope [129–131]. Here the spatial imaging provides the confinement. Figure 17 shows images of distributions of different ionic charge states produced at the focus of a Ti:Sa laser beam. Saturation of ionization is clearly seen in the distributions of  $Ar^+$  and  $Ar^{2+}$  for which around the beam waist, where the intensity is higher, the number of ions drops due to saturation and formation of higher charge states through ionization of  $Ar^+$  and  $Ar^{2+}$ . Details can be found in [131].

An alternative method for the extraction of saturation intensities and hence generalized MP cross-sections is based on the measurement of ponderomotive shifts as a function of the ionizing intensity observed in photoelectron spectra. The saturation intensity is essentially the intensity at which the shift is

saturating. This method has been applied in multi-UV-photon ionization of atoms [138, 139] and it can be extended to the XUV spectral region at high intensity XUV sources [11].

Studies of multi-XUV-photon processes measuring absorption of XUV photons have not been performed so far because absorption in MP processes is a very weak effect. However, recent works [140, 141] indicate that such measurements (e.g. transient absorption measurements) might be feasible. Also, ion and electron spectra so far deal with measurements of total yields. However, ion signals are meanwhile high enough to allow electron/ion imaging methods i.e. measuring angular distributions of products.

Finally, coincidence measurements of products of multi-XUV-photon ionization have not yet been performed because high peak power XUV/attosecond sources so far were low repetition rate (10 Hz) sources, leading to data statistics that are prohibitive for coincidence measurements free of false coincidences. However, new developments of high repetition rate XUV sources (laser based like ELI-ALPS and FELs like Linac Coherent Light Source-LCLS) hold the promise of studies of non-linear XUV processes through coincidence techniques. For such measurements the simplest device, allowing measurement of total yields of products in coincidence, is a time-of-flight spectrometer with time gated repelling voltage. In this way electrons move and reach the detector in a field free environment, while ions remain in the interaction area essentially not moving, and after electrons are detected the ion acceleration voltage is switched on producing the ion mass TOF spectrum. Thus, in the same measured trace, the first part is the electron spectrum and the second one the ion mass spectrum. Keeping the counting rate in single event detection mode, low enough true coincidences may become dominant. This technique has been applied in the first coincidence measurements of strong-field ionization [140, 143]. The most advanced device for electron-ion coincidence measurements is the Reaction Microscope (ReMi) or Cold Target Recoil Ion Momentum Spectroscopy that uses two spectrometers equipped with position sensitive detectors commonly delay detection line detectors [144, 145] detecting electrons and ions respectively. The device, in combination with data analysis packages, allows the measurement of the three-dimensional momentum vector of a recoiling target ion with high resolution and  $4\pi$  solid angle of detection for kinematically complete or close to complete studies. Such devices are foreseen as end-stations in the ELI-ALPS research infrastructure for XUV-pump-XUV-probe coincidence experiments at 1 kHz repetition rate.

### 3. Applications of non-linear XUV processes

The first applications of non-linear XUV processes trace back around year 2000. Those include pioneering work completed with individual harmonics in the few tens of fs temporal regime, including atomic two- [22], three- [146] and four- [147] XUV-photon ionization, two-XUV-photon double ionization [148, 149] as well as the corresponding 2nd [22] and 4th order AC measurements [147], two-XUV-photon Above Threshold Ionization (ATI) [150] (i.e. the processes in which one photon absorption ionizes the atom and the ejected electron absorbs an additional photon undergoing a continuum-continuum transition) and a FROG based-XUV pulse reconstruction [151].

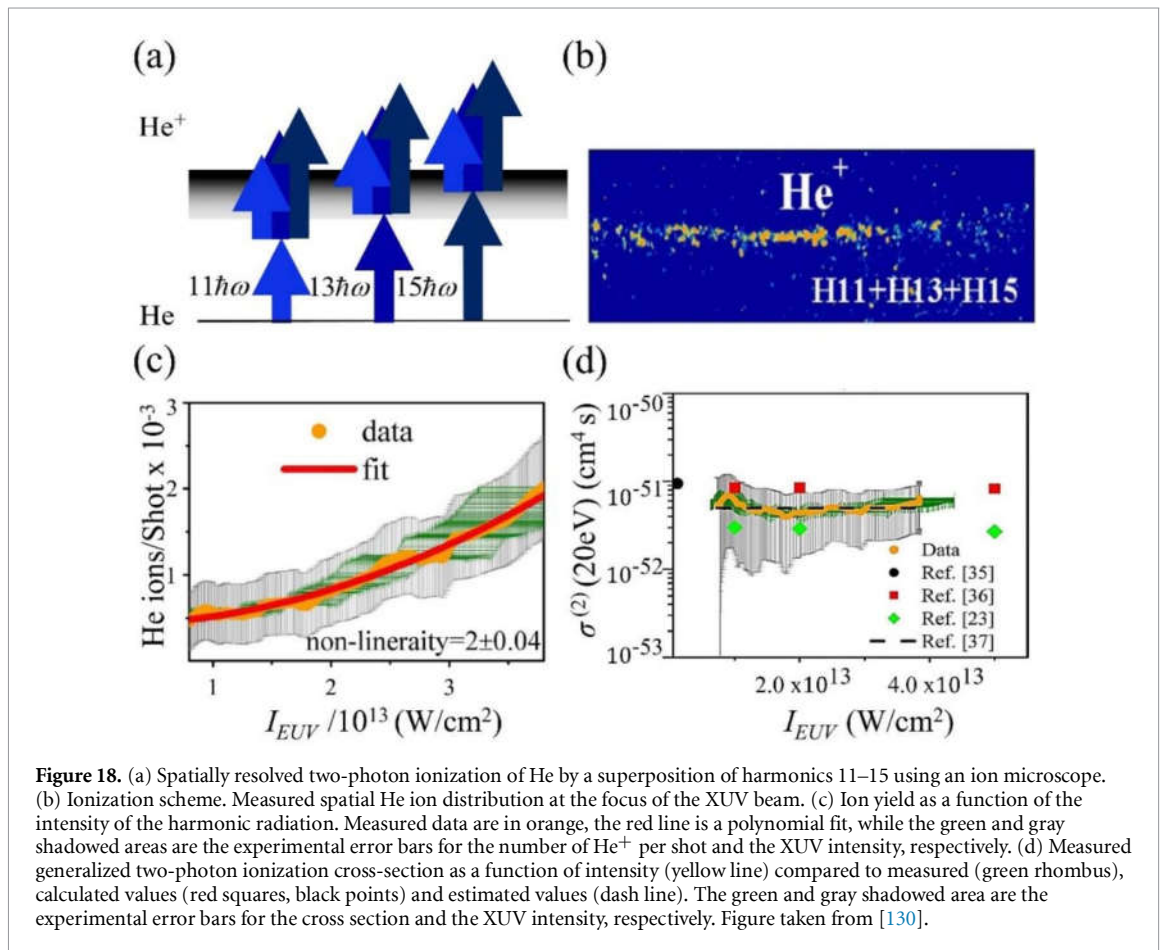
Non-linear XUV applications with a superposition of harmonics, eventually forming attosecond pulse trains, made their debut with the observation of two-photon ionization of He atoms by a superposition of the 7th to the 13th harmonic of a Ti:sapphire laser [111]. The non-linearity of the process was evidenced by the measured slope of the dependence of the ion yield on the ionization XUV radiation intensity in log-log scale. This result was later verified measuring the frequency resolved photoelectron spectra resulting from the same process and comparing it with *ab initio* calculations solving the TDSE of He interacting with the superposition of the four harmonics [134].

Two-XUV-photon double ionization of rare gases by an attosecond pulse train was demonstrated in ionization schemes where the sequential double ionization processes is a three-photon processes (one photon absorption ionizes the atom and absorption of two further photons ionizes the ion) leading to double ionization while the direct one is a two-photon process (absorption of two photons ejects two electrons without intermediate formation of a singly ionized atom) and thus prevails [133]. These works have established the feasibility of non-linear XUV processes induced by laser driven HHG sources. Using advanced detection approaches spatially resolved two-XUV-photon ionization of He by the superposition of harmonics 11–15 was measured exploiting the capabilities of the ion-microscope device [130]. In the work of ref. 129 the generalized two-photon ionization cross section was extracted from one solely measured spatial ion distribution. The main results of this experiment are summarized in figure 18.

More recently multiple multi-XUV-photon processes have been demonstrated in the ionization of Ar [11] and Ne [79] by intense XUV pulses of the 10 GW class harmonic source of FORTH.

Higher non-linearity processes in the XUV and x-ray spectral regions have been observed in FEL infrastructures. Highlighting selected examples: i) formation of very high charge stages of Xe (up to  $\text{Xe}^{21+}$ ) has been demonstrated at the 93 eV photon energy at FLASH and the dependence of the charge state yield on

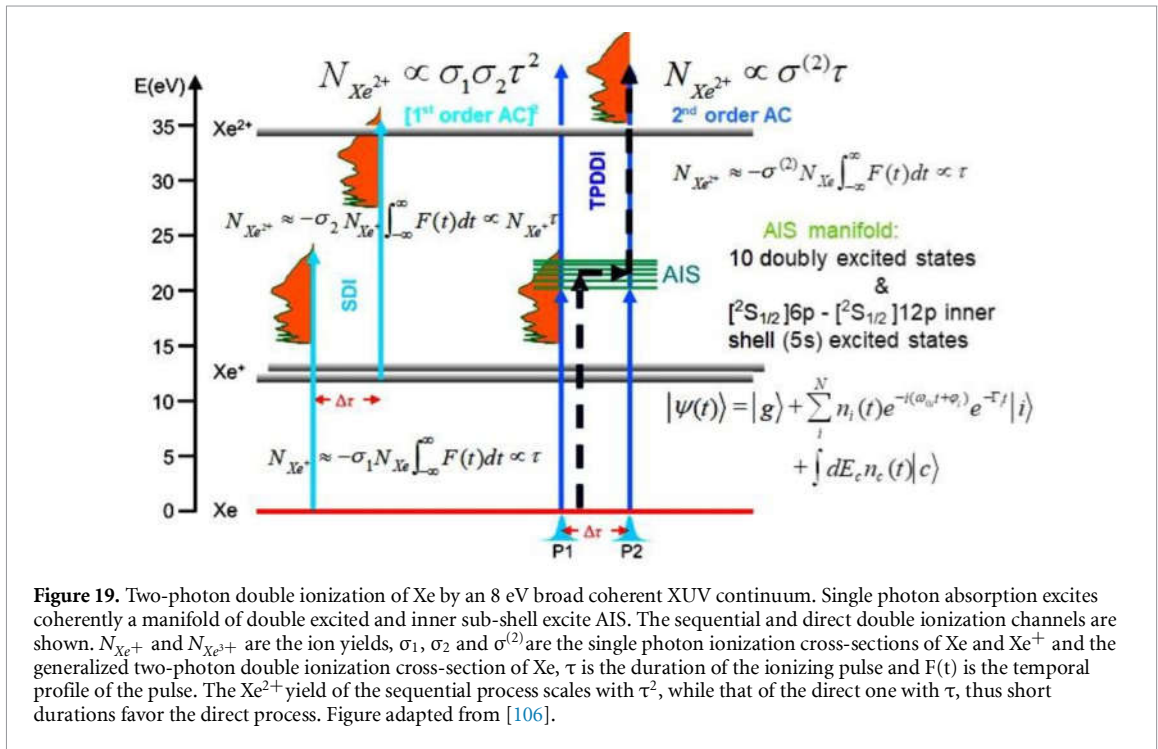




the XUV intensity (up to  $\sim 8 \cdot 10^{15} \text{ W cm}^{-2}$ ) has been measured [152] and interpreted through numerical calculations [65]. The formation of the high charge states is through sequential ionization processes, each of which involves absorption of a large number of photons; ii) ‘coring’ and ‘peeling’ ionization of Ne atoms with photon energies 0.8–2 KeV was demonstrated at LCLS [153]; iii) Formation of Ne<sup>9+</sup> through two-x-ray-photon ionization of Ne<sup>8+</sup> ground state and a high-order sequential process involving single-photon production and ionization of transient excited states on a time scale faster than the Auger decay was studied at LCLS [154]; iv) multiple sequential multi-x-ray-ionization of Xe (up to Xe<sup>36+</sup>) with 80 fs pulses with 2.4–2.6 mJ pulse energy and 1.5 and 2 keV photon energies was demonstrated and x-ray peak fluence dependencies of the ion yields were measured and calculated at LCLS [155]; while v) similar studies have been performed in Xe sequential multiple ionization by 5.5 keV photons and  $47 \mu\text{J}/\mu\text{m}^2$  peak fluence at the Spring-8 Angstrom Compact Free-Electron Laser (SACLA) [156]; vi) two color phase control of ionization was demonstrated at the FERMI FEL, using its fundamental (19.7 eV) and second harmonic (39.4 eV) and varying their relative phase. Quantum interference of single-photon (second harmonic) and two-photon (fundamental) ionization pathways results in phase dependent and thus phase controlled angularly resolved photoelectron yields [157], and vii) two x-ray photon non-sequential absorption of solid targets detecting K-shell fluorescence was reported from SACLA [158, 159].

Investigation of dynamics using pump-probe schemes can optimally be performed exploiting non-linear XUV/x-ray processes. The vast majority of dynamics measured using HHG sources have been performed using hybrid XUV/IR schemes that are beyond the scope of this work as they do not involve any non-linear XUV processes. Hybrid x-ray/optical (see for example [160, 161]) and UV/x-ray (see, for example [162, 163]) pump-probe schemes have been also used in FEL infrastructures and will not be addressed here. x-ray pump-probe studies of picosecond scale dynamics in biological samples have been recently studied in FEL infrastructures (see for example [164]), while the fastest dynamics measured in FEL sources are from the AMO community and are in the 10 fs temporal scale. Those include ultrafast isomerization studies [165] or hetero-site-specific intramolecular dynamics [166].

Experimental investigation of shorter time scales has been conducted exploiting XUV non-linear processes induced by laser driven XUV radiation sources. Thus, two-photon ionization has been used in



performing attosecond pulse train duration measurements via the 2nd IVAC technique discussed in section 2.4. The technique has been applied for the temporal characterization of attosecond trains emitted by the interaction of fs laser pulses with gas targets [121] but also in demonstrating phase locking in CWE surface plasma harmonics forming a *sub-fs* XUV pulse train [95]. In the domain of pulse metrology energy resolved second order AC measurements have also been achieved [167] constituting a step towards pure XUV FROG measurements, while interferometric second order AC traces have been measured in the same year by the same team [168] showing an alternating double to triple peak structure in the trace corresponding to a harmonic field phase change of  $\pi$  between successive peaks that originates from the electron trajectories that are ejected in opposite directions every half laser cycle.

Apart from pulse metrology there have been two works of pure XUV-pump-XUV-probe studies of atomic and molecular dynamics in the 1 fs temporal scale. In both experiments a gold coated split spherical mirror was used as an XUV delay line. In the first one a coherent superposition of AIS of Xe is excited by an 8 eV broad coherent XUV continuum generated through polarization gating of many cycle laser pulses [106, 169], while a second delayed XUV pulse is doubly ionizing the Xe atoms. The ionization scheme, including the sequential and the direct double ionization channel is shown in figure 19 together with the expressions giving the ion yields of the step involved in the two channels. In the work of [106] it was shown that the dominant double ionization process is the direct one. This is because i) the ionizing pulses have ultra-short pulse duration that favours the direct process due to its linear dependence on the pulse duration, in contrast to the quadratic one of the sequential process and ii) the sequential ionization process is mainly a three-photon process and only the tail of the spectrum ionizes sequentially through two-photon absorption.

The dominance of the direct process was verified by the fact that the sequential process would result (in the temporal trace produced by the two mutually delayed XUV pulses) to the square of a first order AC function because each of the steps results a first order AC function, while the direct process results a second order AC function. The width of the square of a first order AC trace is the coherence time of the radiation that can be found through a Fourier transform of the spectrum. The width of a second order AC trace of a Gaussian profile is the pulse duration times the square root of 2. Since the measured temporal width of the trace around zero delay was found much larger than the coherence time of the radiation it was concluded that the direct process is the dominant one.

The measured trace is shown in figure 20. The fast oscillations at longer delays originate from the oscillatory dynamics of the electron wave packet of the coherent superposition of the AIS. The peak around zero delay relates to the pulse duration which though could not be extracted, because the laser carrier-envelope phase (CEP) was not stabilized and thus averaging over several laser pulses creates an overlap of traces produced by single and double pulses, depending on the CEP.

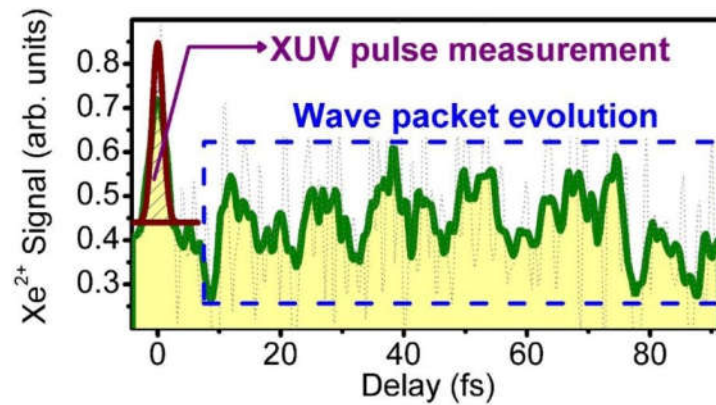


**Figure 20.** Measured temporal trace. The maximum around zero delay relates to the ionizing pulse duration while the oscillatory part of the trace relates to the temporal evolution of the coherently excited AIS manifold. Figure taken from [106].

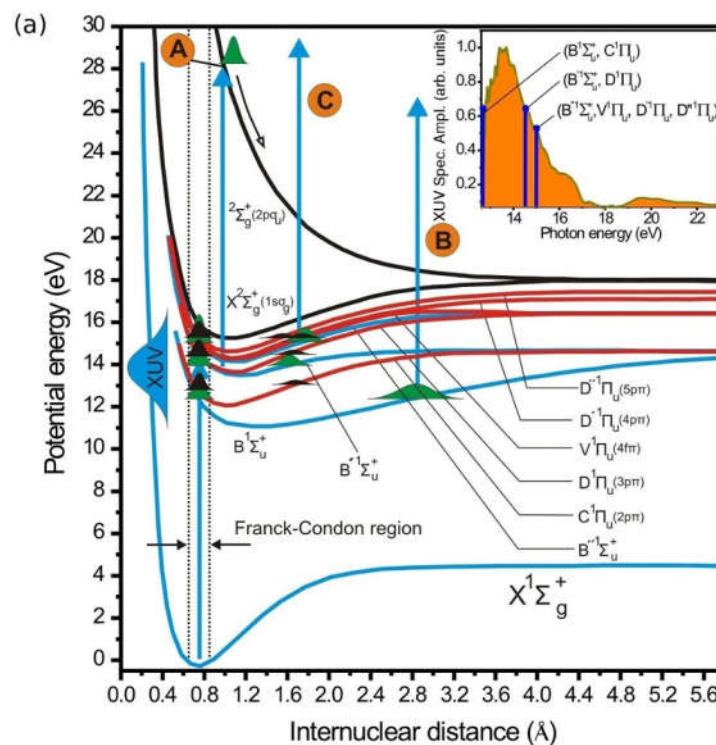


**Figure 21.** Two-photon dissociative ionization scheme of  $H_2$  by broad coherent XUV continuum radiation. The XUV-pump-XUV-probe measurement reveals dissociative ionization, electron and vibrational wavepacket dynamics. The inset shows the bandwidth of the XUV radiation used and the excited intermediate electronic states of the neutral molecule. Figure taken from [122].

A second XUV-pump-XUV-probe experiment at 1 fs time scale was performed in molecular hydrogen [122]. The ionization scheme is shown in figure 21. One photon absorption from a broad coherent XUV continuum excites coherently all the electric dipole allowed electronic bound states of  $H_2$  that are within the Franck-Condon region creating a superposition of electronic and vibrational wave packets (rotational wave packets are not considered here because of their much slower dynamics). A second delayed pulse is ionizing the molecule in the electronic ground state of the ion. After  $\sim 1$  fs the molecule is stretched such that the channel to the dissociative ionization continuum  $2\Sigma_g^+(2p\sigma_u)$  (repulsive potential) is opened (Process A in figures 21). B and C in figure 22 refer to the vibrational dynamics in the  $B^1\Sigma_u^+$  (B) and  $C^1\Pi_u/B^1\Sigma_u^+/D^1\Pi_u$  (C) intermediate electronic states of the neutral molecule. The opening of the dissociative ionization channel after  $\sim 1$  fs was revealed in the measured trace as at zero delay a minimum was observed in the proton yield and this yield is maximized after approximately 1 fs. Vibrational wavepacket dynamics were observed at longer delays. One measured pump-probe trace and its Fourier around 1 fs reveals the opening of the channel. The high peak in the Fourier transform (blue curve) corresponds to the vibrational wavepacket

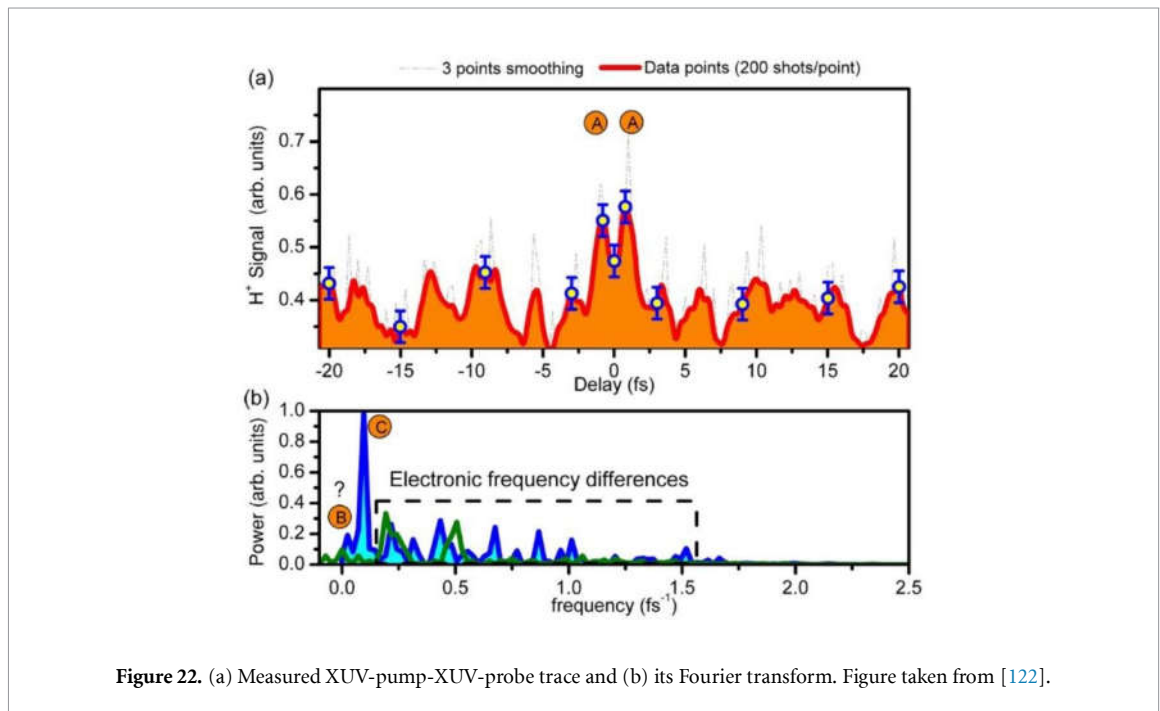


Figure 22. (a) Measured XUV-pump-XUV-probe trace and (b) its Fourier transform. Figure taken from [122].

dynamics in the state, while the high frequency peaks are potentially electronic coherences but their low intensity did not allow a firm assignment.

The experimental conditions under which the XUV-pump-XUV-probe experiments reported so far have the following two disadvantages. First, the many cycle high peak power driving laser pulses were not CEP stabilized. This prohibits the evaluation of the pulse duration of the XUV pulses and reduces the contrast of the oscillatory features of the measured coherences in the temporal trace. CEP tagging is one approach that overcomes this disadvantage; however, no such experiments have been reported so far. The second disadvantage is the low repetition rate (10 Hz) of the laser used, as few tens of mJ pulse energies at higher repetition rates have been only very recently developed. The low repetition rate in turn prohibits coincidence measurements between interaction products (electron–electron, electron-ion, ion-ion) keeping important details of the investigation hidden.

Very recent developments in laser technologies effectively eliminate both shortcomings. Indeed, CEP stabilized multi-10mJ laser systems are becoming available commercially. One such system, the so called SYLOS 2 A system, is already installed at the ELI-ALPS Research Infrastructure. This system is planned to drive two gas targets and one solid target HOHG generation beamlines. The CEP stabilization together with the expected high XUV photon flux of these attosecond beamlines and the availability of advanced experimental end-stations for coincidence measurements enable rigorous attosecond pulse metrology approaches and kinematically complete experiments utilizing non-linear XUV optics at attosecond temporal resolution.

#### 4. Conclusions

Non-linear XUV/x-ray optics made their debut in the beginning of the century. Such processes are central in the investigation of ultrafast dynamics through pump-probe approaches as well as in ultrashort pulse metrology. Since the XUV/x-ray spectral region supports ultrashort pulse synthesis down to the attosecond regime, multi-XUV/x-ray photon processes offer a highly valuable tool in the study of sub-fs dynamics, such as electron dynamics in all states of matter. Moreover, these spectral regions give access to inner-shell dynamics and, eventually, side selective investigation, providing high spatial resolution. Since their debut continuous efforts in source and related instrumentation development have generated notable scientific results and have stimulated new theoretical challenges. While the first non-linear processes have been demonstrated in the XUV spectral region by individual harmonics of fs laser radiation, soon it became feasible to induce them by a superposition of harmonics as well as by coherent continua, thus enabling studies with sub-fs temporal resolution. Few years later FEL sources emitting x-ray pulses with unprecedented photon fluxes gave access to inner-shell investigations and induced highly non-linear processes. In the first 20 years of non-linear processes, laser based harmonic sources and FEL sources played a complementary role, harmonic sources serving the XUV spectral region at the highest temporal resolution

and FEL sources offering unique brilliance in the x-ray and hard x-ray spectral region. Today the sub-fs regime is becoming available at FEL sources and harmonic sources enter the x-ray regime, still the highest temporal resolution of the order of 100 asec is being a feature of harmonic sources, while highest peak power of the order of 100 GW in the x-ray region remains a unique feature of FEL sources. Open technology challenges, where substantial progress was made lately, are the reduction of jitter in pump—probe set-ups, beam pointing stability, CEP stabilization and high repetition rate in high peak-power laser systems. These developments together with innovative imaging and coincidence diagnostic tools boost the capabilities of non-linear XUV/x-ray optics, foreshadowing optimal perspectives for advanced studies of structural dynamics in gas, liquid and condensed phase with highest ever spatio-temporal resolution. In this work we have reviewed non-linear XUV/x-ray processes with emphasis to those induced by laser driven sources, those being our main expertise component in this topic.

## Acknowledgments

We acknowledge support of this work by ‘HELLAS-CH’ (MIS Grant No. 5002735) [which is implemented under the ‘Action for Strengthening Research and Innovation Infrastructures,’ funded by the Operational Program ‘Competitiveness, Entrepreneurship and Innovation’ (NSRF 2014–2020) and co-financed by Greece and the European Union (European Regional Development Fund)], the European Union’s Horizon 2020 research ELI-ALPS is supported by the European Union and cofinanced by the European Regional Development Fund (GINOP Grant Nos. 2.3.6-15-2015-00001), the LASERLAB- EUROPE (EC’s Seventh Framework Programme Grant No. 284464), the Hellenic Foundation for Research and Innovation (HFRI) and the General Secretariat for Research and Technology (GSRT) under grant agreements [GAICPEU (Grant No 645)] and the HFRI PhD Fellowship grant (GA. no. 4816). Funding from the Bundesministerium für Bildung und Forschung (Project 05K19VF1) is gratefully acknowledged. We thank G. Konstantinidis and G. Deligiorgis from the Materials and Devices Division of FORTH-IESL for their support in maintaining the quality of the optical components

## ORCID iDs

I Lontos  <https://orcid.org/0000-0003-0195-0123>  
E Skantzakis  <https://orcid.org/0000-0003-3896-9856>  
B Major  <https://orcid.org/0000-0001-5981-340X>  
S Kahaly  <https://orcid.org/0000-0001-7600-3310>  
K Varju  <https://orcid.org/0000-0001-6577-7417>  
L A A Nikolopoulos  <https://orcid.org/0000-0002-5996-5400>  
D Charalambidis  <https://orcid.org/0000-0002-6468-5868>

## References

- [1] Seddon E A *et al* 2017 *Rep. Prog. Phys.* **80** 115901
- [2] Jahn O *et al* 2019 *Optica* **6** 280
- [3] Duris J *et al* 2020 *Nat. Photon.* **14** 30–36
- [4] Maroju P *et al* 2020 *Nature* **578** 386–91
- [5] Landau L D, Lifšic E M, Landau L D, Lifšits E M, Sykes J B and Bell J S 1977 *Quantum Mechanics: Non-relativistic Theory/Non-relativistic Theory* ed L D Landau and E M Lifšitz 3rd edn (Oxford: Butterworth-Heinemann) vol 3
- [6] Keldysh L V 1965 *Sov. Phys. JETP* **20** 1307–14
- [7] Lambropoulos P 1985 *Phys. Rev. Lett.* **55** 2141–4
- [8] Müller H-G and Fedorov M V 1996 *Super-intense Laser-atom Physics IV (NATO ASI Series. 3, High Technology)* vol 3 (Dordrecht: Kluwer Academic)
- [9] Agostini P and Dimauro L F 2012 Atomic and molecular ionization dynamics in strong laser fields: from optical to x-rays *Advances in Atomic, Molecular, and Optical Physics* ed P R Berman *et al* (New York: Academic) vol 61 pp 117–58
- [10] Ott C *et al* 2019 *Phys. Rev. Lett.* **123** 163201
- [11] Nayak A *et al* 2018 *Phys. Rev. A* **98** 66
- [12] Abel M J, Pfeifer T, Nagel P M, Boutu W, Bell M J, Steiner C P, Neumark D M and Leone S R 2009 *Chem. Phys.* **366** 9–14
- [13] Altucci C *et al* 2010 *Opt. Lett.* **35** 2798–800
- [14] Coster D and Kronig R D L 1935 *Physica* **2** 13–24
- [15] McPherson A, Gibson G, Jara H, Johann U, Luk T S, McIntyre I A, Boyer K and Rhodes C K 1987 *J. Opt. Soc. Am. B* **4** 595
- [16] Ferray M, Lhuillier A, Li X F, Lompre L A, Mainfray G and Manus C 1988 *J. Phys. B: At. Mol. Opt. Phys.* **21** L31–35
- [17] Göppert-Mayer M 1931 *Ann. Phys.* **401** 273–94
- [18] Voronov G S and Delone N B 1965 *JETP Lett.* **1** 66–8
- [19] Voronov G S, Delone G A and Delone N B 1966 *JETP Lett.* **3** 313
- [20] Chatziathanasiou S, Kahaly S, Skantzakis E, Sansone G, Lopez-Martens R, Haessler S, Varju K, Tsakiris G, Charalambidis D and Tzallas P 2017 *Photonics* **4** 26
- [21] Nayak A *et al* 2019 *Phys. Rep.* **833** 1–52

- [22] Kobayashi Y, Sekikawa T, Nabekawa Y and Watanabe S 1998 *Opt. Lett.* **23** 64
- [23] Trebino R 2000 *Frequency-Resolved Optical Gating: The Measurement of Ultrashort Laser Pulses* (New York: Springer)
- [24] Carpeggiani P et al 2017 *Nat. Photon.* **11** 383–9
- [25] Iaconis C and Walmsley I A 1998 *Opt. Lett.* **23** 792–4
- [26] Paul P M, Toma E S, Breger P, Mullot G, Auge F, Balcou P, Muller H G and Agostini P 2001 *Science* **292** 1689–92
- [27] Mairesse Y and Quéré F 2005 *Phys. Rev. A* **71** 803
- [28] Chini M, Gilbertson S, Khan S D and Chang Z 2010 *Opt. Express* **18** 13006–16
- [29] Spanner M, Bertrand J B and Villeneuve D M 2016 *Phys. Rev. A* **94** 023825
- [30] Eckle P, Smolarski M, Schlup P, Biegert J, Staudte A, Schöffler M, Muller H G, Dörner R and Keller U 2008 *Nat. Phys.* **4** 565–70
- [31] Pedatzur O et al 2019 *Nat. Photon.* **13** 91–95
- [32] Constant E, Taranukhin V D, Stolow A and Corkum P B 1997 *Phys. Rev. A* **56** 3870–8
- [33] Orfanos I, Makos I, Lontos I, Skantzakis E, Förg B, Charalambidis D and Tzallas P 2019 *APL Photon.* **4** 80901
- [34] Kruse J E, Tzallas P, Skantzakis E, Kalpouzos C, Tsakiris G D and Charalambidis D 2010 *Phys. Rev. A* **82** 021402(R)
- [35] Gruson V et al 2016 *Science* **354** 734–8
- [36] Drescher M, Hentschel M, Kienberger R, Uiberacker M, Yakovlev V, Scrinzi A, Westerwalbesloh T, Kleineberg U, Heinzmann U and Krausz F 2002 *Nature* **419** 803–7
- [37] Uiberacker M et al 2007 *Nature* **446** 627–32
- [38] Goulielmakis E et al 2004 *Science* **305** 1267–9
- [39] Itatani J, Levesque J, Zeidler D, Niikura H, Pépin H, Kieffer J C, Corkum P B and Villeneuve D M 2004 *Nature* **432** 867–71
- [40] Haessler S et al 2010 *Nat. Phys.* **6** 200–6
- [41] Cavalieri A L et al 2007 *Nature* **449** 1029–32
- [42] Huppert M, Jordan I, Baykusheva D, von Conta A and Wörner H J 2016 *Phys. Rev. Lett.* **117** 93001
- [43] Biswas S et al 2020 *Nat. Phys.* **16** 778–83
- [44] Goulielmakis E et al 2010 *Nature* **466** 739–43
- [45] Calegari F et al 2014 *Science* **346** 336–9
- [46] Kraus P M et al 2015 *Science* **350** 790–5
- [47] Beaulieu S et al 2017 *Science* **358** 1288–94
- [48] Palacios A, González-Castrillo A and Martín F 2014 *Proc. Natl Acad. Sci. USA* **111** 3973–8
- [49] Skantzakis E, Tzallas P, Kruse J E, Kalpouzos C, Faucher O, Tsakiris G D and Charalambidis D 2010 *Phys. Rev. Lett.* **105** 43902
- [50] Eramo R, Cavalieri S, Corsi C, Lontos I and Bellini M 2011 *Phys. Rev. Lett.* **106** 213003
- [51] Dreissen L S, Roth C, Gründeman E L, Krauth J J, Favier M and Eikema K S E 2019 *Phys. Rev. Lett.* **123** 143001
- [52] Palacios A, Horner D A, Rescigno T N and McCurdy C W 2010 *J. Phys. B: At. Mol. Opt. Phys.* **43** 194003
- [53] Kurka M et al 2009 *J. Phys. B: At. Mol. Opt. Phys.* **42** 141002
- [54] Kurka M et al 2010 *New J. Phys.* **12** 73035
- [55] Karule E 1971 *J. Phys. B: At. Mol. Phys.* **4** L67-L70
- [56] Lambropoulos P and Tang X 1987 *J. Opt. Soc. Am. B* **4** 821
- [57] Madsen L B and Lambropoulos P 1999 *Phys. Rev. A* **59** 4574–9
- [58] Allen L and Eberly J H 1975 *Monographs and Texts in Physics and Astronomy* (New York: Wiley)
- [59] Beers B L and Armstrong L 1975 *Phys. Rev. A* **12** 2447–54
- [60] Shore B W 1990 *The Theory of Coherent Atomic Excitation* (New York: Wiley)
- [61] Hanks W, Costello J and Nikolopoulos L 2017 *Appl. Sci.* **7** 294
- [62] Emmanouilidou A, Hakobyan V and Lambropoulos P 2013 *J. Phys. B: At. Mol. Opt. Phys.* **46** 111001
- [63] Nikolopoulos L A A 2003 *Comput. Phys. Commun.* **150** 140–65
- [64] Nakajima T and Nikolopoulos L A A 2002 *Phys. Rev. A* **66** 64
- [65] Makris M G, Lambropoulos P and Mihelic A 2009 *Phys. Rev. Lett.* **102** 33002
- [66] Cowan R D 1981 *The Theory of Atomic Structure and Spectra (Los Alamos Series in Basic and Applied Sciences)* (Berkeley, CA: University of California Press)
- [67] Brown A C, Armstrong G S J, Benda J, Clarke D D A, Wragg J, Hamilton K R, Mašín Z, Gorfinkiel J D and van der Hart H W 2020 *Comput. Phys. Commun.* **250** 107062
- [68] Tulsy V and Bauer D 2020 *Comput. Phys. Commun.* **251** 107098
- [69] Mašín Z, Benda J, Gorfinkiel J D, Harvey A G and Tennyson J 2020 *Comput. Phys. Commun.* **249** 107092
- [70] Lambropoulos P 1976 Topics in multiphoton processes in atoms *Advances in Atomic and Molecular Physics*, ed D R Bates and B Bederson (New York: Academic) pp 87–164
- [71] Georges A T and Lambropoulos P 1979 *Phys. Rev. A* **20** 991–1004
- [72] Nikolopoulos G M and Lambropoulos P 2012 *Phys. Rev. A* **86** 033420
- [73] Lecompte C, Mainfray G, Manus C and Sanchez F 1974 *Phys. Rev. Lett.* **32** 265–8
- [74] Spasibko K Y, Kopylov D A, Krutyanskiy V L, Murzina T V, Leuchs G and Chekhova M V 2017 *Phys. Rev. Lett.* **119** 223603
- [75] Wahlstroem C-G, Larsson J, Persson A, Starczewski T, Svanberg S, Salières P, Balcou P and L’Huillier A 1993 *Phys. Rev. A* **48** 4709–20
- [76] Quintard L et al 2019 *Sci. Adv.* **5** eaau7175
- [77] Chatziathanasiou S, Kahaly S, Charalambidis D, Tzallas P and Skantzakis E 2019 *Opt. Express* **27** 9733
- [78] Heyl C M et al 2016 *Optica* **3** 75
- [79] Makos I et al 2020 *Sci. Rep.* **10** 3759
- [80] Hergott J-F, Kovacev M, Merdji H, Hubert C, Mairesse Y, Jean E, Breger P, Agostini P, Carré B and Salières P 2002 *Phys. Rev. A* **66** 021801(R)
- [81] Rivas D E et al 2018 *Optica* **5** 1283
- [82] Kühn S et al 2017 *J. Phys. B: At. Mol. Opt. Phys.* **50** 132002
- [83] Villorosi P, Bonora S, Pascolini M, Poletto L, Tondello G, Vozzi C, Nisoli M, Sansone G, Stagira S and de Silvestri S 2004 *Opt. Lett.* **29** 207–9
- [84] Altucci C, Bruzese R, D’Antuoni D, de Lisio C and Solimeno S 2000 *J. Opt. Soc. Am. B* **17** 34
- [85] Quéré F, Thauray C, Monot P, Dobosz S, Martin P, Geindre J-P and Audebert P 2006 *Phys. Rev. Lett.* **96** 125004
- [86] Thauray C et al 2007 *Nat. Phys.* **3** 424–9
- [87] Malvache A, Borot A, Quéré F and Lopez-Martens R 2013 *Phys. Rev. E* **87** 035101

- [88] Vincenti H, Monchocé S, Kahaly S, Bonnaud G, Martin P and Quéré F 2014 *Nat. Commun.* **5** 3403
- [89] Dromey B et al 2007 *Phys. Rev. Lett.* **99** 85001
- [90] Baeva T, Gordienko S and Pukhov A 2006 *Phys. Rev. E* **74** 46404
- [91] Gordienko S, Pukhov A, Shorokhov O and Baeva T 2004 *Phys. Rev. Lett.* **93** 115002
- [92] Bulanov S V, Naumova N M and Pegoraro F 1994 *Phys. Plasmas* **1** 745–57
- [93] Tarasevitch A, Lobov K, Wünsche C and von der Linde D 2007 *Phys. Rev. Lett.* **98** 103902
- [94] Dromey B et al 2006 *Nat. Phys.* **2** 456–9
- [95] Nomura Y et al 2008 *Nat. Phys.* **5** 124–8
- [96] Hörlein R et al 2010 *New J. Phys.* **12** 43020
- [97] Gonoskov A A, Korzhimanov A V, Kim A V, Marklund M and Sergeev A M 2011 *Phys. Rev. E* **84** 46403
- [98] Edwards M R and Mikhailova J M 2020 *Sci. Rep.* **10** 5154
- [99] Mondal S, Wei Q, Fareed M A, Hafez H A, Ropagnol X, Sun S, Kahaly S and Ozaki T 2020 *Phys. Rev. Appl.* **13** 034044
- [100] Mondal S et al 2018 *J. Opt. Soc. Am. B* **35** A93
- [101] Kahaly S, Monchocé S, Vincenti H, Dzelzainis T, Dromey B, Zepf M, Martin P and Quéré F 2013 *Phys. Rev. Lett.* **110** 175001
- [102] Tsakiris G D, Eidmann K, Meyer-ter-vehn J and Krausz F 2006 *J. Opt. Soc. Am. B* **8** 19
- [103] Vincenti H 2019 *Phys. Rev. Lett.* **123** 105001
- [104] Karbstein F, Blinne A, Gies H and Zepf M 2019 *Phys. Rev. Lett.* **123** 91802
- [105] Tzallas P, Skantzakis E, Kalpouzou C, Benis E P, Tsakiris G D and Charalambidis D 2007 *Nat. Phys.* **3** 846–50
- [106] Tzallas P, Skantzakis E, Nikolopoulos L A A, Tsakiris G D and Charalambidis D 2011 *Nat. Phys.* **7** 781–4
- [107] Motoyama H, Sato T, Iwasaki A, Takei Y, Kume T, Egawa S, Hiraguri K, Hashizume H, Yamanouchi K and Mimura H 2016 *Rev. Sci. Instrum.* **87** 51803
- [108] Poletto L, Frassetto F, Calegari F, Anumula S, Trabattoni A and Nisoli M 2013 *Opt. Express* **21** 13040–51
- [109] Campi F, Coudert-Alteirac H, Miranda M, Rading L, Manschwetus B, Rudawski P, L’huillier A and Johnsson P 2016 *Rev. Sci. Instrum.* **87** 23106
- [110] Kirkpatrick P and Baez A V 1948 *J. Opt. Soc. Am.* **38** 766–74
- [111] Papadogiannis N A, Nikolopoulos L A A, Charalambidis D, Tsakiris G D, Tzallas P and Witte K 2003 *Phys. Rev. Lett.* **90** 133902
- [112] Goulielmakis E, Nersisyan G, Papadogiannis N A, Charalambidis D, Tsakiris G D and Witte K 2002 *Appl. Phys. B* **74** 197–206
- [113] Papadogiannis N A, Nersisyan G, Goulielmakis E, Rakitzis T P, Hertz E, Charalambidis D, Tsakiris G D and Witte K 2002 *Opt. Lett.* **27** 1561–3
- [114] Pascolini M, Bonora S, Giglia A, Mahne N, Nannarone S and Poletto L 2006 *Appl. Opt.* **45** 3253–62
- [115] Poletto L 2004 *Appl. Phys. B* **78** 1013–6
- [116] Poletto L and Villoresi P 2006 *Appl. Opt.* **45** 8577–85
- [117] Poletto L, Villoresi P, Benedetti E, Ferrari F, Stagira S, Sansone G and Nisoli M 2007 *Opt. Lett.* **32** 2897–9
- [118] Poletto L 2009 *Appl. Opt.* **48** 4526–35
- [119] Poletto L, Villoresi P, Frassetto F, Calegari F, Ferrari F, Lucchini M, Sansone G and Nisoli M 2009 *Rev. Sci. Instrum.* **80** 123109
- [120] Constant E, Mével E, Zair A, Bagnoud V and Salin F 2001 *J. Phys.* **11** Pr2-537–540
- [121] Tzallas P, Charalambidis D, Papadogiannis N A, Witte K and Tsakiris G D 2003 *Nature* **426** 267–71
- [122] Carpeggiani P A, Tzallas P, Palacios A, Gray D, Martín F and Charalambidis D 2014 *Phys. Rev. A* **89** 023420
- [123] Faucher O, Tzallas P, Benis E P, Kruse J, Peralta Conde A, Kalpouzou C and Charalambidis D 2009 *Appl. Phys. B* **97** 505–10
- [124] Tzallas P, Charalambidis D, Papadogiannis N A, Witte K and Tsakiris G D 2005 *J. Mod. Opt.* **52** 321–38
- [125] Wöstmann M, Mitzner R, Noll T, Røling S, Siemer B, Siewert F, Eppenhoff S, Wahlert F and Zacharias H 2013 *J. Phys. B: At. Mol. Opt. Phys.* **46** 164005
- [126] Kolliopoulos G, Tzallas P, Bergues B, Carpeggiani P A, Heissler P, Schröder H, Veisz L, Charalambidis D and Tsakiris G D 2014 *J. Opt. Soc. Am. B* **31** 926
- [126] Treusch R 2005 *HASYLAB Annual Report 2005 DESY (2005)*
- [127] Tiedke K 2003 *HASYLAB Annual Report 2003 DESY (2003)*
- [129] Kolliopoulos G, Bergues B, Schröder H, Carpeggiani P A, Veisz L, Tsakiris G D, Charalambidis D and Tzallas P 2014 *Phys. Rev. A* **90** 013822
- [130] Tsatrafyllis N et al 2016 *Sci. Rep.* **6** 21556
- [131] Tzallas P, Bergues B, Rompotis D, Tsatrafyllis N, Chatziathanassiou S, Muschet A, Veisz L, Schröder H and Charalambidis D 2018 *J. Opt.* **20** 024018
- [132] Dacasa H et al 2019 *Opt. Express* **27** 2656–70
- [133] Benis E P, Charalambidis D, Kitsopoulos T N, Tsakiris G D and Tzallas P 2006 *Phys. Rev. A* **74** 051402(R)
- [134] E P B, Tzallas P, Nikolopoulos L A A, Kovačev M, Kalpouzou C, Charalambidis D and Tsakiris G D 2006 *New J. Phys.* **8** 92
- [135] Wagner M and Schröder H 1993 *Int. J. Mass Spectrom. Ion Process.* **128** 31–45
- [136] Schröder H, Wagner M, Kaesdorf S and Kompa K L 1993 *Ber. Bunsen Ges. Phys. Chem.* **97** 1688–91
- [137] Laude L D 1994 *Excimer Lasers* (Dordrecht: Springer)
- [138] Charalambidis D, Xenakis D, Uiterwaal C J G J, Maragakis P, Zhang J, Schröder H, Faucher O and Lambropoulos P 1997 *J. Phys. B: At. Mol. Opt. Phys.* **30** 1467–79
- [139] Uiterwaal C J G J, Xenakis D, Charalambidis D, Maragakis P, Schröder H and Lambropoulos P 1998 *Phys. Rev. A* **57** 392–400
- [140] Tsatrafyllis N, Kominis I K, Gonoskov I A and Tzallas P 2017 *Nat. Commun.* **8** 15170
- [141] Tsatrafyllis N et al 2019 *Phys. Rev. Lett.* **122** 193602
- [142] Witzel B, Papadogiannis N A and Charalambidis D 2000 *Eur. Phys. J. D* **12** 21–25
- [143] Witzel B, Papadogiannis N A and Charalambidis D 2000 *Phys. Rev. Lett.* **85** 2268–71
- [144] Dörner R, Mergel V, Jagutzki O, Spielberger L, Ullrich J, Moshhammer R and Schmidt-Böcking H 2000 *Phys. Rep.* **330** 95–192
- [145] Ullrich J, Moshhammer R, Dorn A, Dörner R, Schmidt L P H and Schmidt-Böcking H 2003 *J. Phys. B: At. Mol. Opt. Phys.* **66** 1463–545
- [146] Descamps D, Roos L, Delfin C, L’huillier A and Wahlström C-G 2001 *Phys. Rev. A* **64** 273
- [147] Sekikawa T, Ohno T, Yamazaki T, Nabekawa Y and Watanabe S 1999 *Phys. Rev. Lett.* **83** 2564–7
- [148] Nabekawa Y, Hasegawa H, Takahashi E J and Midorikawa K 2005 *Phys. Rev. Lett.* **94** 43001
- [149] Manschwetus B et al 2016 *Phys. Rev. A* **93** 061402(R)
- [150] Miyamoto N, Kamei M, Yoshitomi D, Kanai T, Sekikawa T, Nakajima T and Watanabe S 2004 *Phys. Rev. Lett.* **93** 83903
- [151] Sekikawa T, Katsura T, Miura S and Watanabe S 2002 *Phys. Rev. Lett.* **88** 193902

- [152] Sorokin A A, Bobashev S V, Feigl T, Tiedtke K, Wabnitz H and Richter M 2007 *Phys. Rev. Lett.* **99** 213002
- [153] Young L *et al* 2010 *Nature* **466** 56–61
- [154] Doumy G *et al* 2011 *Phys. Rev. Lett.* **106** 83002
- [155] Rudek B *et al* 2012 *Nat. Photon.* **6** 858–65
- [156] Fukuzawa H *et al* 2013 *Phys. Rev. Lett.* **110** 173005
- [157] Prince K C *et al* 2016 *Nat. Photon.* **10** 176–9
- [158] Tamasaku K *et al* 2014 *Nat. Photon.* **8** 313–6
- [159] Ghimire S, Fuchs M, Hastings J, Herrmann S C, Inubushi Y, Pines J, Shwartz S, Yabashi M and Reis D A 2016 *Phys. Rev. A* **94** 043418
- [160] Glowonia J M *et al* 2010 *Opt. Express* **18** 17620–30
- [161] Canton S E *et al* 2015 *Nat. Commun.* **6** 6359
- [162] Wolf T J A *et al* 2017 *Nat. Commun.* **8** 29
- [163] Squibb R J *et al* 2018 *Nat. Commun.* **9** 63
- [164] Levantino M, Schirò G, Lemke H T, Cottone G, Glowonia J M, Zhu D, Chollet M, Ihee H, Cupane A and Cammarata M 2015 *Nat. Commun.* **6** 6772
- [165] Liekhus-Schmaltz C E *et al* 2015 *Nat. Commun.* **6** 8199
- [166] Picón A *et al* 2016 *Nat. Commun.* **7** 11652
- [167] Nabekawa Y, Shimizu T, Okino T, Furusawa K, Hasegawa H, Yamanouchi K and Midorikawa K 2006 *Phys. Rev. Lett.* **96** 83901
- [168] Nabekawa Y, Shimizu T, Okino T, Furusawa K, Hasegawa H, Yamanouchi K and Midorikawa K 2006 *Phys. Rev. Lett.* **97** 153904
- [169] Skantzakis E, Tzallas P, Kruse J, Kalpouzos C and Charalambidis D 2009 *Opt. Lett.* **34** 1732–4